PONTIFICIA UNIVERSIDAD CATÓLICA DE CHILE
ESCUELA DE INGENIERÍA

NON-CONFORMING FINITE ELEMENTS SCHEMES FOR CARDIAC MODELING

JAVIERA JILBERTO VALLEJOS

Thesis submitted to the Office of Research and Graduate Studies
in partial fulfillment of the requirements for the degree of
Master of Science in Engineering

Advisor:
DANIEL HURTADO

Santiago de Chile, November 2018

PONTIFICIA UNIVERSIDAD CATÓLICA DE CHILE
ESCUELA DE INGENIERÍA

NON-CONFORMING FINITE ELEMENTS SCHEMES FOR CARDIAC MODELING

JAVIERA JILBERTO VALLEJOS

Members of the Committee:
DANIEL HURTADO
ELWIN VAN'T WOUT
CHRISTOPHER COOPER
DANI GUZMÁN

Thesis submitted to the Office of Research and Graduate Studies
in partial fulfillment of the requirements for the degree of
Master of Science in Engineering

Santiago de Chile, November 2018

To my parents, Ximena and José, for always being there for me.

ACKNOWLEDGEMENTS

I wish to thank my advisor, Daniel Hurtado, for his guidance, advice and support, from the first course where he was my teacher, Introduction to Biomechanics. His constant motivation and challenges showed me a new and exciting path. It has been a pleasure to learn from him and I hope to continue collaborating with him in the future. I also wish to thank to the members of the commission, Elwin Van'T Wout, Christopher Cooper and Dani Guzmán, for their time and comments during the thesis development.

During the two years of my master's studies, I had the support and advice of my partners at the laboratory Mauricio Sarabia, Carlos Andrade, William Ramírez, David Ortiz, Patricio Zavala, Felipe Álvarez, Agustín Pérez and Pablo Bascuñan. I want to thank them for that and for the pleasant place to work they gave me.

I also want to thank to the game of basketball and all the beautiful people I knew thanks to it. The seven years that I spent studying at Pontificia Universidad Católica de Chile would not have been the same without my friends in the University's team. I thank each of them for never letting me fall or quit and for all these years and moments that I will never forget.

Finally, I want to thank my family for their support during all these years. To my brother Felipe, and my sister, Ximena, for their understanding, company and advice. Special thanks to my parents, Ximena Vallejos and José Jilberto, because no matter which path I took or what problem I faced, they never left me alone, and they gave me the love and support I needed.

TABLE OF CONTENTS

LIST OF FIGURES

LIST OF TABLES

ABSTRACT

The field of computational cardiology has steadily progressed toward reliable and accurate simulations of the heart, showing great potential in clinical applications such as the optimization of cardiac interventions and the study of pro-arrhythmic effects of drugs in humans, among others. However, the computational effort demanded by in-silico studies of the heart remains prohibitively high, highlighting the need for novel numerical methods that can improve the efficiency of simulations while targeting an acceptable accuracy from a physiological viewpoint, a trade-off typically found in computer simulations. In this work, we propose a semi-implicit non-conforming finite-element scheme (SI-NCFES) suitable for cardiac electrophysiology simulations. The proposed scheme is assessed by means of numerical simulations of electrical excitation in regular and biventricular geometries, where we show that, based on coarse discretizations, it can predict with high accuracy the wavefront shape and conduction velocity at a fraction of the computing time demanded by standard simulations based on fine discretizations. We further show that the SI-NCFES allows for coarse discretizations of cardiac domains while being physiologically accurate for simulations of spiral wave dynamics, which are otherwise not feasible using standard finite-element formulations, thus improving the accuracy-efficiency trade-off of cardiac simulations of arrhythmia.

Keywords: Non-conforming Finite Elements, Computational Cardiology, Cardiac Electrophysiology, Conduction Velocity, Nonlinear Finite Elements

RESUMEN

La cardiología computacional ha tenido un progreso constante en lo que se refiere a lograr simulaciones confiables y precisas del corazón, mostrando un gran potencial en aplicaciones clínicas como la optimización de intervenciones cardíacas y el estudio del efecto pro-arritmia de drogas en humanos, entre otras. Sin embargo, el esfuerzo computacional que los estudios *in-silico* del corazón demandan sigue siendo un desafío, lo que remarca la necesidad de nuevos métodos numéricos que puedan mejorar la eficiencia de las simulaciones pero que mantengan una precisión aceptable. En este trabajo, proponemos un método semi-implícito no-conforme de elementos finitos (SINCFES) para simulaciones de electrofisiología cardíaca. La precisión y eficiencia del método propuesto son evaluadas en términos de simulaciones numéricas de la excitación y propagación eléctrica en geometrías regulares y en un dominio biventricular. Con estas simulaciones demostramos que SINCFES permite el uso de mallas más gruesas que reducen el tiempo computacional en comparación con modelos de mallas finas entregando frentes de onda y velocidades de conducción más precisas que aquellas predecidas por las formulaciones tradicionales de elementos finitos con la misma malla gruesa, mejorando la relación precisión-eficiencia de las simulaciones cardíacas.

Keywords: elementos finitos no-conformes, cardiología computacional, electrofisiología cardíaca, velocidad de conducción, elementos finitos no-lineales.

1. INTRODUCTION

1.1. Motivation

Since the past decades the role of mathematics has led to important advances in the development of medical technologies and in advancing the understanding of physiological phenomena. Today, there are several physiological systems of the human body that can be described in mathematical terms, which allows for *in-silico* simulations that help scientists from different disciplines to draw conclusions about normal and pathological processes in the body. Several examples of physiology process described in terms of mathematical functions can be found in Keener and Sneyd (2009a, 2009b).

In the study of the functioning of the heart, computational cardiology has made great advances due to the improvement of biophysical models and computational tools. Currently, it is possible to model the electrical activity of the whole heart and obtain medical conclusions from computational simulations (Trayanova, Boyle, & Nikolov, 2018; Sahli Costabal, Yao, & Kuhl, 2018). However, these computational tools need further development before they can be used for health applications by medical professionals. Because of the complexity and non-linearity of the electrophysiology equations, numerical schemes are necessary to solve them. Finite difference, finite volume and finite elements (FE) methods have been used with this purpose (Colli Franzone et al., 2014). The latter is the most widely used method, and is the one we adopt in this work. When using FE, due to the nature of the equations, it is necessary to use a small spatio-temporal discretization that results in a high computational cost. Thus, one of the main challenges of computational cardiology is to decrease the computational effort that these simulations take without losing their predictive capability (Sundnes et al., 2006).

In the search of efficient numerical methods for computational cardiology, Hurtado and Rojas Hurtado and Rojas (2018) recently proposed a novel non-conforming finite element scheme (NCFES), and proved that this method allows for the use of coarser meshes that translated into lower computational costs without compromising accuracy. However, they

used an implicit, Backward Euler scheme to integrate the equations over time. Despite implicit methods allow for large time steps, they are very costly in terms of computational effort, since several linear-system solves are needed for each time step. The purpose of this work is to develop a scheme following the same principles of using non-conforming elements but with a more efficient time-integration scheme.There are several options to choose from when selecting a time integration scheme (Colli Franzone et al., 2014). In our case we chose a semi-implicit scheme which is a simpler option and has shown to significantly reduce the computational cost (Whiteley, 2006; Pathmanathan et al., 2010).

1.2. Thesis Structure

This thesis consist of four chapters, the first one presents an introduction to the research and the theoretical framework in which is based. The second chapter is the paper associated to this thesis entitled ”Semi-implicit non-conforming finite-element schemes for cardiac electrophysiology: a framework for mesh-coarsening heart simulations”, which has been recently published in the journal Frontiers in Physiology. The third chapter presents the conclusions and the fourth, the future extensions related to the present work.

1.3. Cardiac Electrophysiology

The importance of the heart is well known, as it is the organ responsible for pumping blood through our body. The heart is composed by four chambers, two atria and two ventricles. The blood enters the atria and then is pumped towards the ventricles which drive the blood to the lungs (right side) to oxygenate it or to the circulatory system (left side). Figure 1.1 illustrates the anatomy of the heart and how the blood passes through.

At a cellular level, the heart is composed by and extracellular matrix and millions of cardiac muscle cells, also known as cardiomyocytes, that contract and relax following a certain

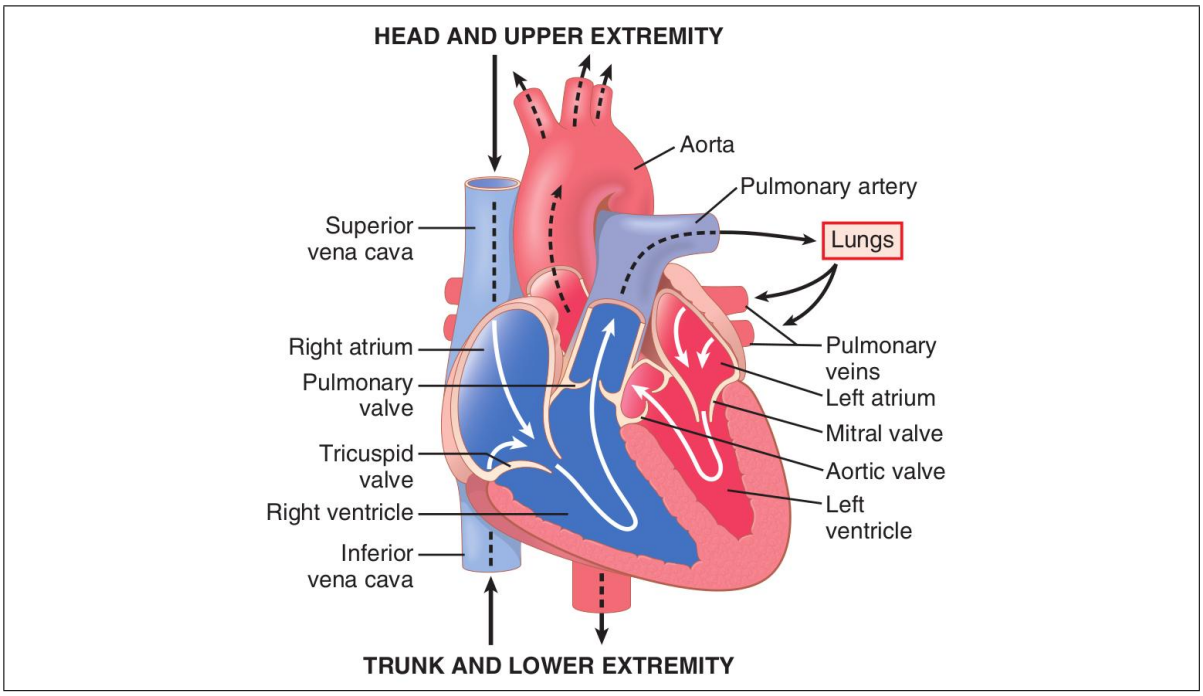

Figure 1.1. Heart anatomy showing the four chambers and the blood flux. Taken from Guyton and Hall (2016).

complex pattern that is controlled by electrical activation. Cardiomyocytes have the characteristic of not only be contractile, but also electrically excitable, as they enable the propagation of an electric potential. The electrical activation of the heart is not homogeneous, since it is mediated by different types of structures formed by cells with different characteristics. Some of this structures are the atrio-ventricular node (AVN), the bundle of His or the Purkinje network. The cells in the AVN, for example, have a relatively small conduction which is responsible for the delay in the activation time of the ventricles respect to the atria (Colli Franzone et al., 2014).

At the tissue level, cells are arranged following an specific direction as shown in Figure 1.2. This direction is called the *fiber axis*. The fibers are embeded in sheets, in where it is defined the *sheet axis*. A third direction called *cross-sheet axis* is defined as the cross product of the other two (Castro, 2015). To facilitate the propagation in the fiber axis, at

the union between two cells there are specialized structures called gap junctions that allow a facilitated flux of ions. The fiber organization in the heart makes the tissue anisotropic as the conduction will be faster in the direction of the fibers. It is important to note that it is possible to distinguish three different layers across the heart walls. From the external to the internal wall these layers are the epicardium, mid-myocardium and endocardium. This layered structure is important for electrical conduction, since the orientation of the fibers changes along the thickness of these layers.

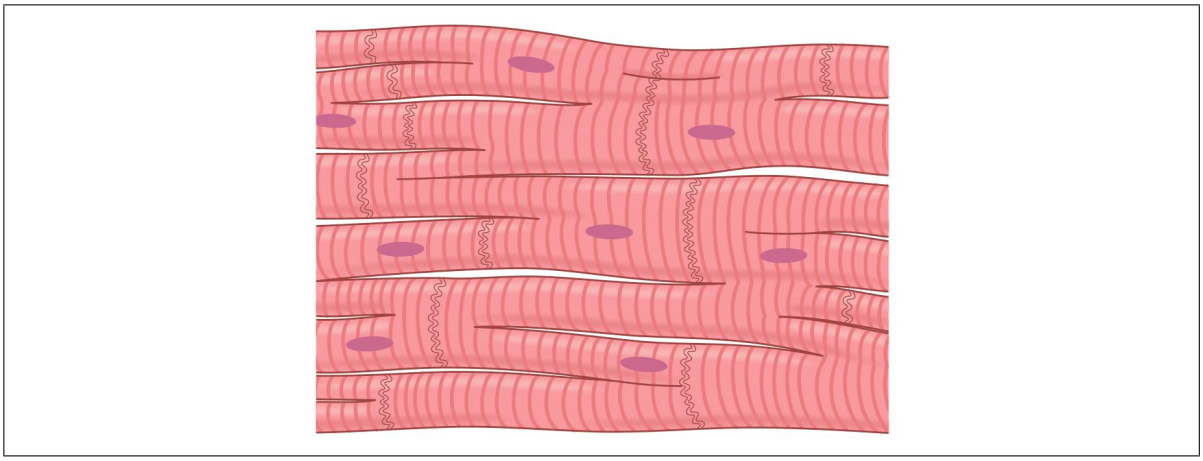

Figure 1.2. Heart tissue illustration. Taken from Guyton and Hall (2016).

As briefly explained in this section, the electrical conductivity in the heart is a complex process that presents diverse challenges. It is also known that most of the heart diseases are the result or a cause of abnormal electrical behavior (Sundnes et al., 2006). For these reasons, there is an important source of questions that computational cardiology can help to answer. In the following sections a mathematical description of the physiology of the heart is presented to develop equations that can be solved using numerical schemes.

1.3.1. Single Cell Potential

A very important feature of cardiac cells is that they are excitable. This means that given a certain electrical stimulus the cell will answer actively. If no stimulus is applied, then the cell membrane maintains an internal ionic concentration that is different from the external one. Due to the charge of the ions, this concentration difference results in a difference of the electrical potential. This is called transmembrane potential V_{m} and is defined by:

$$V_{\mathrm{m}} = \phi_{\mathrm{i}} - \phi_{\mathrm{e}},$$

where ϕ_{i} is the potential in the intracellular space, and ϕ_{e} is the potential in the extracellular space. Under resting conditions, the transmembrane potential in cardiomyocytes is about -85 mV. For a cell in resting conditions, if a stimulus with a value below a certain threshold is applied, the cell will rapidly return to its resting condition. If the stimulus is larger than a certain threshold value, the cell will change its membrane conductive properties, and a flux of positive ions will enter the cell, a process that is known as depolarization. After depolarization occurs, the transmembrane potential will return to its resting value in a process called repolarization. In cardiac cells, unlike other excitable cells, this process is slow due to a momentary equilibrium in the in and out flow of charges which is reflected in the so-called plateau phase (Pullan, Cheng, & Buist, 2005). In Figure 1.3, the phases of the cardiac potential and the interaction of the four most important ionic currents (Na^+, Cl^-, K^+, Ca^{2+}) are plotted, and it is possible to observe that depolarization is a very fast process.

The behavior of the cell membrane can be represented as an electrical circuit, see Figure 1.4. The current flow for an specific ion x is governed by the difference between the transmembrane potential and the Nerst potential E_x of that ion. Hence, the expression for the current through a channel I_x is

$$I_x = g_x(V_{\mathrm{m}} - E_x),$$

where g_x is the conductance of the channels for that ion. Because the conductance usually depends on both the transmembrane potential and the concentration levels of other ions, g_x is assumed to be a nonlinear function. Since the conductances are arranged in parallel the

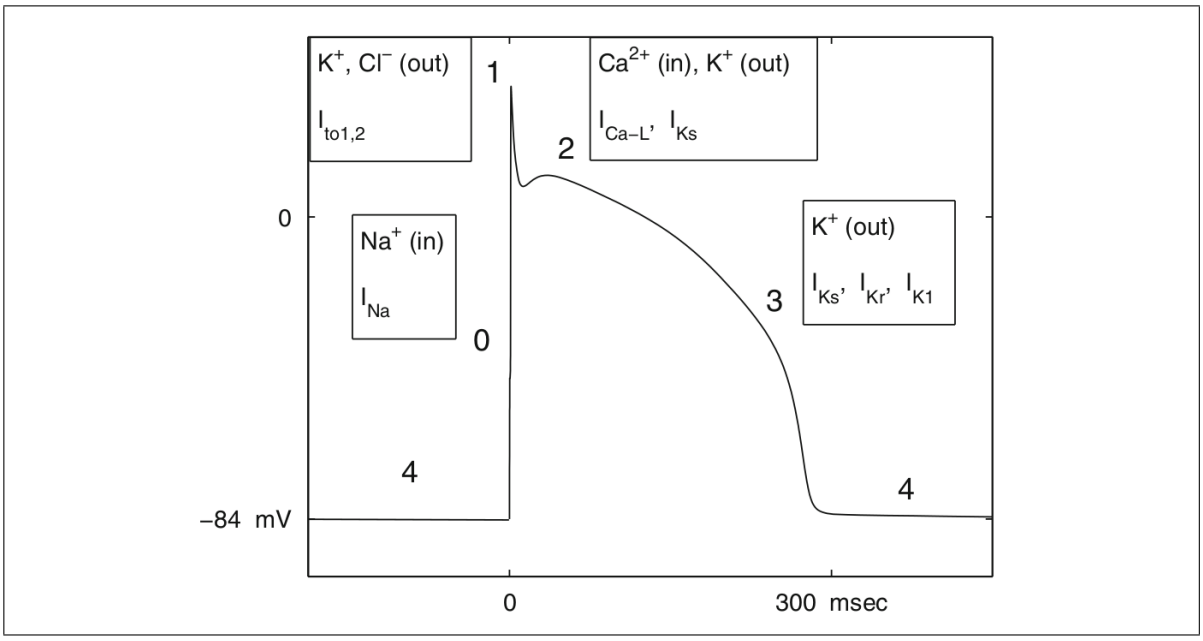

Figure 1.3. Schematic of the cardiac action potential. Phase 0 (depolarization or upstroke), phase 1 (peak), phase 2 (plateau), phase 3 (repolarization or recovery) and ionic currents involved in each phase are shown. Taken from (Colli Franzone et al., 2014).

currents through each channel can be sum linearly to obtain I_{ion} which is the total current flowing through the ions channels,

$$I_{\text{ion}} = \sum_{x} I_x.$$

Since the cell membrane separates charges that accumulate in the intracellular and extracellular spaces, it can be idealized as a capacitor with capacitance C_{m} which is placed parallel to the ionic currents. This electrical circuit representation yields to the following expression for the transmembrane potential over time,

$$C_{\text{m}} \frac{\partial V_{\text{m}}}{\partial t} + I_{\text{ion}} = I_{\text{app}},$$

where I_{app} is an externally applied current (Pullan et al., 2005; Sundnes et al., 2006; Colli Franzone et al., 2014).

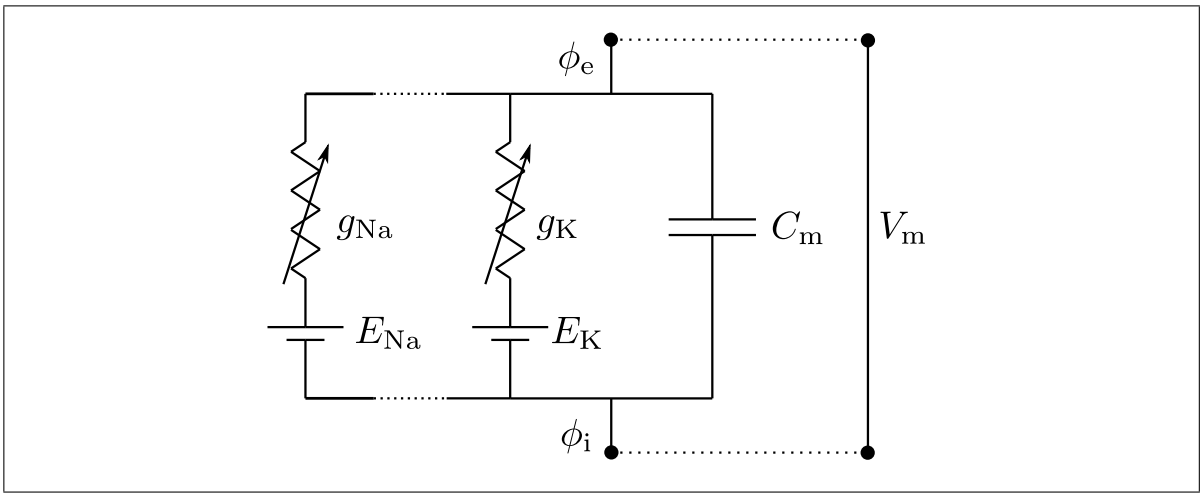

Figure 1.4. Electrical circuit representing the flow of current across the cell membrane.

The functions that represent each ionic current I_x change according to the ionic model used. The first mathematical model proposed to represent the electrical cell behavior was the Hodgkin-Huxley model (Hodgkin & Huxley, 1952) of the squid giant axon. The Hodgkin-Huxley model separates the total ionic transmembrane current into three components: the sodium current I_{Na}, the potassium current I_{K}, and a leakage current I_{L} that represent all other ions. Based on the Hodgkin-Huxley model, several ionic models have been developed in the past to represent the electrical behavior of the cardiac cells, both for human hearts as well as for hearts from several animal species. These models vary both in complexity and in if they have a biophysical basis or phenomenological basis. Biophysical models tends to be more elaborated, and may have more than ten gating variables in order to represent each ionic channel (Tusscher, Noble, Noble, & Panfilov, 2004). In contrast, phenomenological models are simpler because they do not seek to represent the sub-cellular process but rather to provide a phenomenological representation of an action potential, at a minimum computational cost. A review on the main models used in literature can be found on Pullan et al. (2005) or on Colli Franzone et al. (2014). In this work, we used the Aliev-Panfilov model (Aliev & Panfilov, 1996) which belongs to the phenomenological group, and is described in detail in Chapter 2.

1.3.2. Signal Conduction

To be able to represent the propagation of an action potential across the cell membrane, the cell is generally modeled as a long cylindrical cable in which the transmembrane potential only depends on the length variable and not on radial or angular variables. This is the so-called *core conductor assumption* (Colli Franzone et al., 2014; Keener & Sneyd, 2009a). The cable is assumed to be composed of isopotential membrane sections of length dx. An electrical circuit representation of this model is presented in Figure 1.5. The axial intracellular

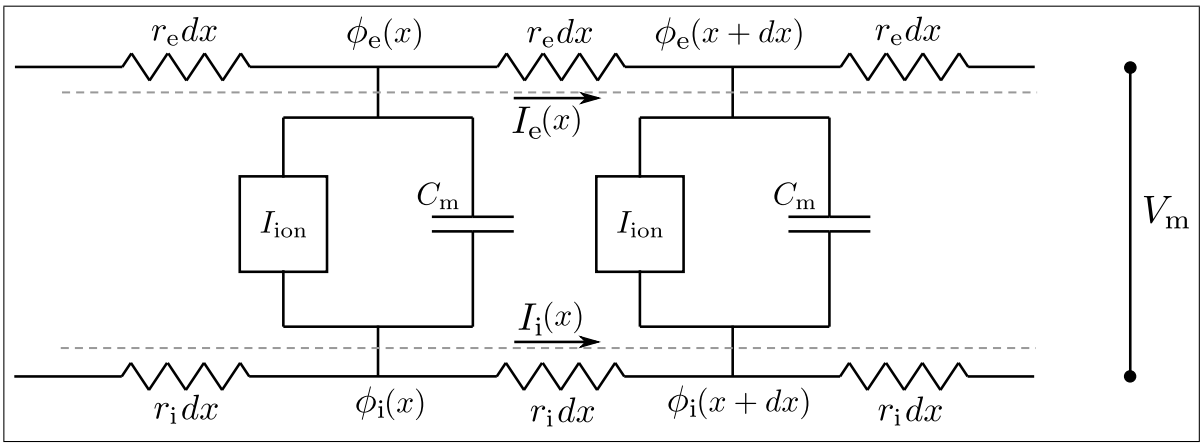

Figure 1.5. Equivalent circuit representation used to derive the cable equation. The membrane is shown between the dashed lines separating the intracellular from the extracellular space.

and extracellular current is assumed to be ohmic, i.e.,

$$\phi_i(x+dx) - \phi_i(x) = -I_i(x) r_i dx,$$

$$\phi_e(x+dx) - \phi_e(x) = -I_e(x) r_e dx,$$

where r_{i} and r_{e} are the resistances per unit length. Then, in the limit when $dx \to 0$ we have that

$$I_{\mathrm{i}}(x) = -\frac{1}{r_{\mathrm{i}}}\frac{\partial \phi_{\mathrm{i}}}{\partial x}, \tag{1.1}$$

$$I_{\mathrm{e}}(x) = -\frac{1}{r_{\mathrm{e}}}\frac{\partial \phi_{\mathrm{e}}}{\partial x}. \tag{1.2}$$

From Kirchhoff's laws, we have that the changes in the extracellular or in the intracellular axial current are due to the transmembrane current I_{t},

$$I_{\mathrm{i}}(x) - I_{\mathrm{i}}(x+dx) = I_{\mathrm{t}}dx = I_{\mathrm{e}}(x+dx) - I_e(x). \tag{1.3}$$

In the limit $dx \to 0$, the latter becomes

$$I_t = -\frac{\partial I_{\mathrm{i}}}{\partial x} = \frac{\partial I_{\mathrm{e}}}{\partial x}. \tag{1.4}$$

The total axial current is $I_{\mathrm{T}} = I_{\mathrm{i}} + I_{\mathrm{e}}$ and we know that $V_{\mathrm{m}} = \phi_{\mathrm{i}} - \phi_{\mathrm{e}}$. Combining this two and (1.1) and (1.2) and reordering we get

$$-I_{\mathrm{i}} = \frac{1}{r_{\mathrm{i}} + r_{\mathrm{e}}}\frac{\partial V_{\mathrm{m}}}{\partial x} - \frac{r_{\mathrm{e}}}{r_{\mathrm{i}} + r_{\mathrm{e}}} I_{\mathrm{T}}. \tag{1.5}$$

Taking the partial derivative from x and using (1.4) and the fact that I_{T} is constant we obtain:

$$I_{\mathrm{t}} = \frac{\partial}{\partial x}\left(\frac{1}{r_{\mathrm{i}} + r_{\mathrm{e}}}\frac{\partial V_{\mathrm{m}}}{\partial x}\right). \tag{1.6}$$

We further note that the current per unit of area i_t can be written as

$$i_t = C_{\mathrm{m}}\frac{\partial V_{\mathrm{m}}}{\partial t} + I_{\mathrm{ion}},$$

and it can be expressed as current per unit volume if we multiply by the ratio between the membrane surface area for a given length to the volume enclosed by this surface A_{m}, i.e.,

$$I_t = A_{\mathrm{m}}\left(C_{\mathrm{m}}\frac{\partial V_{\mathrm{m}}}{\partial t} + I_{\mathrm{ion}}\right). \tag{1.7}$$

From (1.6) and (1.7) we get the cable equation

$$A_{\mathrm{m}}\left(C_{\mathrm{m}}\frac{\partial V_{\mathrm{m}}}{\partial t}+I_{\mathrm{ion}}\right)-\sigma\frac{\partial^2 V_{\mathrm{m}}}{\partial x^2}=0, \tag{1.8}$$

where σ is the effective conductivity, which can be shown to be (Colli Franzone et al., 2014)

$$\sigma=\frac{\sigma_{\mathrm{i}}\sigma_{\mathrm{e}}}{\sigma_{\mathrm{i}}+\sigma_{\mathrm{e}}}=\frac{1}{\rho_{\mathrm{i}}+\rho_{\mathrm{e}}}, \tag{1.9}$$

with σ_{i} and σ_{e} the external and internal conductivities respectively. Here we use the fact that the resistivities ρ are the resistance r multiplying a certain lenght and dividying by the area of the cable. It is possible to extrapolate the cable equation to a multidimensional space using a conductivity tensor $\boldsymbol{\sigma}$ (Castro, 2015),

$$A_{\mathrm{m}}\left(C_{\mathrm{m}}\frac{\partial V_{\mathrm{m}}}{\partial t}+I_{\mathrm{ion}}\right)-\mathrm{div}(\boldsymbol{\sigma}\nabla V_{\mathrm{m}})=0. \tag{1.10}$$

For convenience, the cable equation is typically normalized (Rojas, 2017). We define the normalized transmembrane potential ϕ as

$$\phi(\boldsymbol{x},t)=\frac{V_{\mathrm{m}}(\boldsymbol{x},t)-V_{\mathrm{r}}}{V_{\mathrm{p}}-V_{\mathrm{r}}}.$$

Further, we divide (1.10) by $A_{\mathrm{m}}C_{\mathrm{m}}$ to obtain

$$\frac{\partial\phi}{\partial t}-\mathrm{div}(\boldsymbol{D}\nabla\phi)-f(\phi,\boldsymbol{r})=0, \tag{1.11}$$

where $f(\phi,\boldsymbol{r})$ is the normalized ionic current and $\boldsymbol{D}$ is the normalized conductivity tensor, both which can be related to their counterparts by

$$\boldsymbol{D}=\frac{1}{A_{\mathrm{m}}C_{\mathrm{m}}}\boldsymbol{\sigma};\qquad f(\phi,\boldsymbol{r})=-\frac{I_{\mathrm{ion}}(V_{\mathrm{m}}(\phi),\boldsymbol{r})}{C_{\mathrm{m}}(V_{\mathrm{p}}-V_{\mathrm{r}})}$$

As already mentioned, the term I_{ion} is the sum of the contribution to the total current of all ions and will depend on V_{m} and on the concentration levels of other ions. In mathematical terms we write $I_{\mathrm{ion}}=I_{\mathrm{ion}}(V_{\mathrm{m}},\boldsymbol{r})$, where $\boldsymbol{r}$ is a vector containing the state variables which

vary in time according to the following equation

$$\frac{\partial \boldsymbol{r}}{\partial t} = g(\phi, \boldsymbol{r}) \tag{1.12}$$

1.4. Semi-Discrete Finite-Element Formulation for the Cable Model

To solve the cable equation using finite elements in a certain domain $\Omega \in \mathbb{R}^3$, it is first necessary to start from a weak formulation. To this end, we define the function spaces

$$\mathcal{S} = \{\phi(\boldsymbol{x}) \in H^1(\Omega, \mathbb{R}) | \phi(\boldsymbol{x}) = \phi_g \text{ if } \boldsymbol{x} \in \partial\Omega_g\},$$
$$\mathcal{V} = \{\nu(\boldsymbol{x}) \in H^1(\Omega, \mathbb{R}) | \nu(\boldsymbol{x}) = 0 \text{ if } \boldsymbol{x} \in \partial\Omega_g\},$$

where $\mathcal{S}$ is the trial space, $\mathcal{V}$ is the test space, H^1 is the Sobolev space and ϕ_g are the prescribed potentials (Dirichlet condition) and Ω_g is the Dirichlet boundary. Multiplying (1.11) b y an arbitrary function $\nu \in \mathcal{V}$, integrating over the whole domain Ω, and using integration by parts we arrive to the weak form:
Find $\phi \in \mathcal{S}$ such that $\forall\ t \in (0, T]$

$$\int_\Omega \nu\dot{\phi}\ \mathrm{d}x + \int_{\partial\Omega_q} \nu\bar{q}\ \mathrm{d}s + \int_\Omega \nabla\nu \cdot \boldsymbol{D}\nabla\phi\ \mathrm{d}x - \int_\Omega \nu f(\phi, \boldsymbol{r})\ \mathrm{d}x = 0 \quad \forall \nu \in \mathcal{V} \tag{1.13}$$

where $\bar{q} = \boldsymbol{q} \cdot \hat{\boldsymbol{n}}$ is the prescribed flux and Ω_q is the Neumann boundary which appears naturally in the deduction.

The weak form can be discretized using a finite element approach. Let us consider a discretization Ω^h of the domain Ω which is composed by elements domains Ω^e such that $\Omega^h = \cup_{e=1}^{N_{\mathrm{el}}} \Omega^e$ where N_{el} is the number of elements. Now, we define

$$\mathcal{S}^h \subset \mathcal{S}; \qquad \mathcal{V}^h \subset \mathcal{V}; \tag{1.14}$$

and approximate ϕ and ν with the functions $\phi^h \in \mathcal{S}$ and $\nu^h \in \mathcal{V}$. Following a traditional finite element scheme, these functions are defined by

$$\nu^h(\boldsymbol{x}) = \sum_{A=1}^{N_{\text{dofs}}} N_A(\boldsymbol{x})\nu_A; \qquad \phi^h(\boldsymbol{x}) = \sum_{A=1}^{N_{\text{dofs}}} N_A(\boldsymbol{x})\phi_A;$$

where N_{dofs} is the number of degrees of freedom present in the discretized domain, ϕ_A and ν_A are the nodal values of the respective fields and $N_A(\boldsymbol{x})$ are basis functions. Using the definition of $\nu^h(\boldsymbol{x})$ into (1.13), we get

$$\int_\Omega N_A \dot{\phi}^h \mathrm{d}x + \int_\Omega \nabla N_A \cdot \boldsymbol{D} \nabla \phi^h \mathrm{d}x - \int_\Omega N_A f(\phi^h, \boldsymbol{r}^h) \mathrm{d}x + \int_{\partial\Omega_q} N_A \bar{q}\, \mathrm{d}s = 0 \qquad A = 1, ..., \mathrm{N}_{\text{dofs}}. \quad (1.15)$$

This last equation is known are the semi-discrete finite element formulation of the problem, where the time domain is still continuous.

1.5. Temporal Integration Schemes

In this section we will present three temporal discretization schemes for the semi-discrete equations (1.15): the Forward Euler (explicit) scheme, the Backward Euler (implicit) scheme, and the semi-implicit scheme. The first two methods are members of the *generalized trapezoidal family of methods* and are widely used in electrophysiology (Colli Franzone et al., 2014). The integration in time of the evolution of the state variables (1.12) will also depend on the scheme adopted. We partition the time interval into $[0, \ldots, t_n, t_{n+1}, \ldots, T]$ intervals, and approximate the time-dependent coefficients $\square(t_n) \approx \square_n$. For a generic time interval $[t_n, t_{n+1}]$ we define $\Delta t := t_{n+1} - t_n$. All the variables with sub-index n are assumed to be known. The time derivatives are replaced by the finite-difference approximation

$$\dot{\square}(t_{n+1}) \approx \frac{\square_{n+1} - \square_n}{\Delta t}. \quad (1.16)$$

1.5.1. Forward Euler Scheme

Using a Forward-Euler scheme, equations (1.12) and (1.15) are discretized in time as

$$\int_\Omega N_A \frac{\phi^h_{n+1} - \phi^h_n}{\Delta t} \mathrm{d}x + \int_\Omega \nabla N_A \cdot \boldsymbol{D} \nabla \phi^h_n \mathrm{d}x - \int_\Omega N_A f(\phi^h_n, \boldsymbol{r}^h_n) \mathrm{d}x + \int_{\partial\Omega_q} N_A \bar{q} \, \mathrm{d}s = 0, \quad (1.17)$$

$$\frac{\boldsymbol{r}^h_{n+1} - \boldsymbol{r}^h_n}{\Delta t} = g(\phi^h_n, \boldsymbol{r}^h_n), \quad (1.18)$$

where we notice that we can express ϕ^h_{n+1} in terms of ϕ^h_n and $\boldsymbol{r}_n$. Using a finite-element approximation for ϕ^h it is possible to rewrite 1.17 in matrix terms

$$\mathbf{M} \frac{\boldsymbol{\phi}_{n+1} - \boldsymbol{\phi}_n}{\Delta t} + \mathbf{K}\boldsymbol{\phi}_n - \mathbf{F}(\boldsymbol{\phi}_n, \boldsymbol{r}_n) = \mathbf{0},$$

where $\boldsymbol{\phi} = [\phi_1, ..., \phi_{N_{\text{nodes}}}]$ is a vector with the nodal values of the normalized transmembrane potential, $\mathbf{M}$, $\mathbf{K}$ are the mass and stiffness matrices, respectively, and $\mathbf{F}$ is the nodal force vector. The entries for the matrix are given by:

$$M_{AB} = \int_\Omega N_A N_B \qquad K_{AB} = \int_\Omega \nabla N_A \cdot \boldsymbol{D} \nabla N_B$$

$$F_A = \int_\Omega N_A f(\phi^h_n, \boldsymbol{r}^h_n) \mathrm{d}x - \int_{\partial\Omega_q} N_A \bar{q} \, \mathrm{d}s$$

Then, the update for $\boldsymbol{\phi}_{n+1}$ is simply

$$\boldsymbol{\phi}_{n+1} = \boldsymbol{\phi}_n - \Delta t \mathbf{M}^{-1}(\mathbf{K}\boldsymbol{\phi}_n - \mathbf{F}(\boldsymbol{\phi}_n, \boldsymbol{r}_n)) \quad (1.19)$$

$$\boldsymbol{r}_{n+1} = \boldsymbol{r}_n + \Delta t g(\boldsymbol{\phi}_n, \boldsymbol{r}_n) \quad (1.20)$$

This method has the advantage of being very simple to implement, together with having a low computational cost, as no iterations is needed to find $\boldsymbol{\phi}_{n+1}$. In particular, it is possible to compute $\mathbf{M}$ and $\mathbf{K}$ only once, and then reuse them in each time step. The main deficiency of this method is that it is conditionally stable, i.e., the time step size is controlled by the mesh size, as the following stability inequality must hold:

$$\Delta t < \frac{2}{\lambda^h_{max}},$$

where λ^h_{max} is the maximum eigenvalue of the matrix $\mathbf{M}^{-1}\mathbf{K}$. This condition forces the use of very small time-step sizes, which can make simulations very expensive from a computational standpoint (Hughes, 2012).

1.5.2. Backward Euler Scheme

Using a Backward-Euler scheme, we define the following residuals using equations (1.12) and (1.15)

$$R^\phi_A(\phi^h, \boldsymbol{r}^h) = \int_\Omega N_A \frac{\phi^h - \phi^h_n}{\Delta t} \mathrm{d}x + \int_\Omega \nabla N_A \cdot \boldsymbol{D} \nabla \phi^h \mathrm{d}x - \int_\Omega N_A f(\phi^h, \boldsymbol{r}^h) \mathrm{d}x + \int_{\partial\Omega_q} N_A \bar{q} \, \mathrm{d}s = 0 \tag{1.21}$$

$$\mathbf{R}^r(\phi^h, \boldsymbol{r}^h) = \boldsymbol{r}^h - \boldsymbol{r}^h_n - \Delta t g(\phi^h, \boldsymbol{r}^h) = \mathbf{0} \tag{1.22}$$

where the sub-index $n+1$ is intentionally omitted for convenience. Since the non-linear terms $f(\phi, \boldsymbol{r})$ and $g(\phi, \boldsymbol{r})$ depend on ϕ^h and $\boldsymbol{r}^h$, it is not possible to directly solve for them. Therefore, it is necessary to use a numerical scheme to solve this set of non-linear equations. One common alternative is to use the Newton's method. To this end, we first solve (1.22), as it does not involve spatial gradients. The tangent matrix is given by

$$D\mathbf{R}^r = \frac{\partial \mathbf{R}^r}{\partial r} = 1 - \Delta t \frac{\partial g}{\partial r}(\phi^h, \boldsymbol{r}^h)$$

Then, given a initial value for $\boldsymbol{r}$, we start updating the value $\boldsymbol{r} \leftarrow \boldsymbol{r} - (D\mathbf{R}^r)^{-1}\mathbf{R}^r$ until a certain criteria on the residual norm is met. The converged value is denoted as $\boldsymbol{r}^*(\phi^h)$. We now turn to the residual for ϕ^h, the tangent matrix is:

$$DR^\phi_{AB} = \frac{\partial R^\phi_A}{\partial \phi_B} = \int_\Omega \frac{1}{\Delta t} N_A N_B \mathrm{d}x + \int_\Omega \nabla N_A \cdot \boldsymbol{D} \nabla N_B \mathrm{d}x - \int_\Omega N_A N_B Df(\phi^h, \boldsymbol{r}^h) \mathrm{d}x$$

where

$$Df = \frac{\mathrm{d}f(\phi^h, r^*(\phi))}{\mathrm{d}\phi} = \left\{ \frac{\partial f}{\partial \phi} + \frac{\partial f}{\partial r} \frac{\mathrm{d}r^*}{\mathrm{d}\phi} \right\} \Bigg|_{\phi^h, r^*}$$

and $\frac{\mathrm{d}r^*}{\mathrm{d}\phi}$ can be obtained using (1.22),

$$\frac{\mathrm{d}r^*}{\mathrm{d}\phi} = -(D\mathbf{R}^r)^{-1}\left(\frac{\partial g}{\partial \phi}\right)\Bigg|_{\phi^h, r^*}$$

Thus, the update for $\boldsymbol{\phi}$ is,

$$\boldsymbol{\phi} \leftarrow \boldsymbol{\phi} - D\mathbf{R}^{\phi^{-1}}\mathbf{R}^{\phi}$$

this iteration is performed until a convergence criteria over the norm of $\mathbf{R}^{\phi}$ is met (Hurtado, Castro, & Gizzi, 2016). The principal advantage of this method is that it provides a larger stability region for the time-step size (Hurtado & Henao, 2014). The main disadvantage of the Backward-Euler method is its complexity and the computational effort that demands the solution of the resulting set of non-linear equations that need to be solved at each time step.

1.5.3. Semi-implicit Scheme

In this method, the diffusion terms are evaluated at the current time step t_{n+1}, and the ionic terms at the previous time step t_n (Whiteley, 2006). Thus, the semi-discrete equations (1.15) turn into

$$\int_\Omega N_A \frac{\phi^h_{n+1} - \phi^h_n}{\Delta t}\mathrm{d}x + \int_\Omega \nabla N_A \cdot \boldsymbol{D}\nabla\phi^h_{n+1}\mathrm{d}x - \int_\Omega N_A f(\phi^h_n, \boldsymbol{r}^h_n)\mathrm{d}x, \\ + \int_{\partial\Omega_q} N_A \bar{q}\,\mathrm{d}s = 0, \quad (1.23)$$

$$\frac{\boldsymbol{r}^h_{n+1} - \boldsymbol{r}^h_n}{\Delta t} = g(\phi^h_n, \boldsymbol{r}^h_n). \quad (1.24)$$

We readily notice the advantage of this method: the ionic functions $f(\phi, \boldsymbol{r})$, $g(\phi, \boldsymbol{r})$ are evaluated at the previous time step where all information is known, and therefore the update of the gating variables results in a straightforward evaluation. Using the matrix approach shown in the Forward Euler scheme we further get,

$$\mathbf{M}\frac{\boldsymbol{\phi}_{n+1} - \boldsymbol{\phi}_n}{\Delta t} + \mathbf{K}\boldsymbol{\phi}_{n+1} - \mathbf{F}(\boldsymbol{\phi}_n, \boldsymbol{r}_n) = \mathbf{0}$$

The equation for $\boldsymbol{r}$ (1.24) is the same than in that found for the case of the Forward-Euler scheme. Then, the updates for $\boldsymbol{\phi}$ and $\boldsymbol{r}$ are:

$$\boldsymbol{\phi}_{n+1} = \boldsymbol{\phi}_n - \left(\frac{\mathbf{M}}{\Delta t} + \mathbf{K}\right)^{-1} (\mathbf{K}\boldsymbol{\phi}_n - \mathbf{F}(\boldsymbol{\phi}_n, \boldsymbol{r}_n)), \tag{1.25}$$

$$\boldsymbol{r}_{n+1} = \boldsymbol{r}_n + \Delta t g(\boldsymbol{\phi}_n, \boldsymbol{r}_n). \tag{1.26}$$

One advantage of this method is that the stability condition does not depend on the mesh size, which allows for time-step sizes larger than those allowed by the explicit schemes.

2. SEMI-IMPLICIT NON-CONFORMING FINITE-ELEMENT SCHEMES FOR CARDIAC ELECTROPHYSIOLOGY

2.1. Introduction

Computer simulations of the electrical activity of the heart have increasingly gained attention in the medical community, as they have steadily shown potential in the study of cardiac diseases and in the design of novel cardiac therapies. Current models of the human heart are able to represent the complex three-dimensional anatomical structure of the heart chambers, incorporating key functional features such as the Purkinje network and the cardiomyocyte orientation (Vadakkumpadan et al., 2009). Such advanced representation of the heart has enabled novel in-silico studies of undesired pro-arrhythmic effects of drugs in patients (Sahli Costabal et al., 2018), potentially reducing the number of subjects needed in a clinical trial by aiding the experiment design. Computational models of the heart have also shown promise in assisting the design of effective therapies for terminating atrial fibrillation (Trayanova et al., 2018). While these examples can only confirm the tremendous relevance of computational models in advancing the field of cardiology, they share the fundamental challenge of being highly demanding in terms of wall-clock time needed in computer simulations.

Mathematical models of the heart require the computer implementation of spatio-temporal discretization techniques in order to obtain a sequence of numerical representations of the physiological fields under study. Two fundamental aspects directly responsible for the computation time (CT) in a heart simulation are the ionic model used to account for subcellular electrochemical mechanisms, and the level of spatio-temporal discretization in terms of time-step size and mesh size (Sundnes et al., 2006). The choice of the mesh size typically faces a well-known trade-off problem of accuracy versus efficiency, as decreasing the mesh size in a simulation results in more accurate numerical approximations, at the cost of increasing the number of degrees of freedom (DOFs), which drives the CT. Indeed, current simulations of the heart typically employ mesh sizes in the range of tens to hundreds of micrometers

for domains with lengths in the order of centimeters, which ultimately translates into large systems of equations with several millions of DOFs that need to be solved at each time step. Such high dimensionality renders the solution of heart simulations extremely challenging for personal computers, and calls for improving their implementation in high-performance computing (HPC) platforms (Vazquez et al., 2011; S. Niederer, Mitchell, Smith, & Plank, 2011).

In the particular case of cardiac electrophysiology simulations, a common criterion to select the mesh size is the ability of the numerical simulation to recover an accurate conduction velocity (CV) and wavefront shape (Pathmanathan et al., 2010; Krishnamoorthi, Sarkar, & Klug, 2013; Dupraz, Filippi, Gizzi, Quarteroni, & Ruiz-Baier, 2015). It has been shown that both the wavefront shape and the CV suffer from a strong dependence on the spatial discretization, which for the case of finite-element (FE) discretization using linear basis functions results in a significant loss of accuracy for the case of mesh sizes $> 0.1\,\mathrm{mm}$ (Pezzuto, Hake, & Sundness, 2016). In order to achieve larger mesh sizes, higher-order FE formulations have been proposed, which show that FE Lagrange basis functions of order 2 and 3 result in accurate CV for coarser meshes (Arthurs, Bishop, & Kay, 2012; Pezzuto et al., 2016). It should be noted, however, that higher-order FE schemes based on Lagrange basis functions necessarily increase the total number of DOFs in simulations when compared to linear-element formulations, as well as they require an additional computational effort for quadrature procedures, as higher-order basis functions demand the use of more quadrature-point evaluations (Cantwell, Yakovlev, Kirby, Peters, & Sherwin, 2014). Recently, (Hurtado & Rojas, 2018) introduced a non-conforming finite-element scheme (NCFES) for the spatial discretization of the monodomain equation of cardiac electrophysiology that allows for the use of coarse meshes without significant loss of accuracy measured in terms of CV and wavefront shape. More specifically, hexahedral trilinear elements (Q1) were enhanced with non-conforming basis functions of degree 2 to create a non-conforming element (Q1NC) that is capable of representing a second-order polynomial within the element domain, a concept widely employed in the context of solid mechanics FE simulations (Wilson, Taylor, Doherty, & Ghaboussi, 1973; Taylor, Beresford, & Wilson, 1976). Further, they showed that the DOFs

associated to the non-conforming basis functions can be solved at the element level, and therefore the number of global DOFs of the Q1NC scheme equals that of a standard Q1 FE scheme. As a result, Q1NC simulations delivered a CV and wavefront shape similar to that of second-order Lagrange formulations (Q2) at the computational cost in the order of a Q1 formulation.

During the development of the NCFES for cardiac electrophysiology, a fully-implicit (FI) backward-Euler time-stepping method was considered (Hurtado & Rojas, 2018). While FI schemes have important advantages in delivering a larger time-step stability region in cardiac simulations (Ying, Rose, & Henriquez, 2008; Hurtado & Henao, 2014), they require the solution of a large system of non-linear equations at each time step that can be very costly in computational terms, and may not be well-suited to parallel-computing platforms when compared to other numerical schemes. To improve the computational efficiency, the semi-implicit integration method has been proposed in the literature for solving the semi-discrete equations resulting from standard FE discretizations, showing a relevant decrease in the CT of cardiac simulations, as well as being amenable to HPC platforms (Whiteley, 2006; Pathmanathan et al., 2010). Consequently, the scientific question that motivates this work is: Can we further improve the efficiency-accuracy trade-off in cardiac simulations by combining non-conforming FE spatial discretizations with semi-implicit time-integration schemes? To answer such question, in the following we develop the numerical framework and present an algorithm for the implementation of a semi-implicit non-conforming FE scheme to solve the monodomain electrophysiology equations, and investigate the numerical consequences and potential contributions to cardiac simulations.

2.2. Methods

2.2.1. Monodomain model of cardiac electrophysiology

Let $\Omega \in \mathbb{R}^3$ be the heart domain where electrical impulses travel during the time interval $[0, T]$, and $V_{\mathrm{m}} : \Omega \times [0, T] \to \mathbb{R}$ be the transmembrane potential. A local statement of current balance yields the monodomain equation (Pullan et al., 2005)

$$A_{\mathrm{m}} \left(C_{\mathrm{m}} \frac{\partial V_{\mathrm{m}}}{\partial t} + I_{\mathrm{ion}}(V_{\mathrm{m}}, \boldsymbol{r}) \right) - \mathrm{div}(\boldsymbol{\sigma} \nabla V_{\mathrm{m}}) = 0, \quad \text{in } \Omega \times (0, T], \tag{2.1}$$

where $A_{\mathrm{m}}, C_{\mathrm{m}}$ are the surface-to-volume ratio and membrane capacitance, respectively, $\boldsymbol{\sigma}$ is the conductivity tensor, I_{ion} is the ionic current depending on the transmembrane potential V_{m}, and $\boldsymbol{r} : \Omega \times (0, T] \to \mathbb{R}^{\mathrm{m}}$ is a vector field of state variables that include gating variables and ion concentrations. For convenience, we consider the normalized transmembrane potential field

$$\phi(\boldsymbol{x}, t) = \frac{V_{\mathrm{m}}(\boldsymbol{x}, t) - V_{\mathrm{r}}}{V_{\mathrm{p}} - V_{\mathrm{r}}},$$

where V_{p} and V_{r} are the peak and resting voltages, respectively. Based on this normalization, we obtain the non-dimensional monodomain equation,

$$\frac{\partial \phi}{\partial t} - \mathrm{div}(\boldsymbol{D} \nabla \phi) - f(\phi, \boldsymbol{r}) = 0 \quad \text{in } \Omega \times (0, T], \tag{2.2}$$

where $\boldsymbol{D} = \frac{1}{A_{\mathrm{m}} C_{\mathrm{m}}} \boldsymbol{\sigma}$ is the normalized conductivity tensor, and $f(\phi, \boldsymbol{r}) = -\frac{I_{\mathrm{ion}}(V_{\mathrm{m}}(\phi), \boldsymbol{r})}{C_{\mathrm{m}}(V_{\mathrm{p}} - V_{\mathrm{r}})}$ is the normalized ionic current. The time evolution of state variables is governed by kinetic equations of the form

$$\frac{\partial \boldsymbol{r}}{\partial t} = g(\phi, \boldsymbol{r}) \quad \text{in } \Omega \times (0, T]. \tag{2.3}$$

The expressions for $f(\phi, \boldsymbol{r})$ and $g(\phi, \boldsymbol{r})$ will depend on the choice of ionic model representing the transmembrane ionic current in a single cell. Equations (2.2) and (2.3) are complemented with Dirichlet and Neumann boundary conditions,

$$\phi = \bar{\phi}, \qquad \text{on } \partial\Omega_\phi \times (0, T], \tag{2.4}$$

$$\boldsymbol{q} \cdot \boldsymbol{n} = \bar{q}, \qquad \text{on } \partial\Omega_q \times (0, T], \tag{2.5}$$

respectively, as well as initial conditions

$$\phi(\boldsymbol{x}, 0) = \phi_0(\boldsymbol{x}), \quad \boldsymbol{x} \in \Omega,$$

$$\boldsymbol{r}(\boldsymbol{x}, 0) = \boldsymbol{r}_0(\boldsymbol{x}), \quad \boldsymbol{x} \in \Omega.$$

To state the weak form of the cardiac electrophysiology problem, we consider trial spaces $\mathcal{S}^\phi, \mathcal{S}^r$ and test spaces $\mathcal{V}^\phi, \mathcal{V}^r$ defined as

$$\mathcal{S}^\phi = \{\phi \in L^2((0,T]; H^1(\Omega, \mathbb{R})) : \ \phi = \bar{\phi} \text{ on } \partial\Omega_\phi \times (0,T]\} \tag{2.6}$$

$$\mathcal{S}^r = \{\boldsymbol{r} \in L^2((0,T]; L^2(\Omega, \mathbb{R}^m))\} \tag{2.7}$$

$$\mathcal{V}^\phi = \{\nu \in H^1(\Omega, \mathbb{R}) : \ \nu = 0 \text{ on } \partial\Omega_\phi\} \tag{2.8}$$

$$\mathcal{V}^r = \{\boldsymbol{\eta} \in L^2(\Omega, \mathbb{R}^m)\} \tag{2.9}$$

Multiplying (2.2) and (2.3) by appropriate test functions, integrating over Ω and applying the divergence theorem yields the weak equations, and the statement of the weak formulation reads: $\forall\, t \in (0,T]$, find $(\phi, \boldsymbol{r}) \in \mathcal{S}^\phi \times \mathcal{S}^r$ such that

$$\begin{aligned} G^\phi[(\phi, \boldsymbol{r}), (\nu, \boldsymbol{\eta})] := &\int_\Omega \nu \frac{\partial \phi}{\partial t} \, \mathrm{d}x + \int_\Omega \nabla\nu \cdot \mathbf{D}\nabla\phi \, \mathrm{d}x \\ &- \int_\Omega \nu f(\phi, r) \, \mathrm{d}x + \int_{\partial\Omega_q} \nu \bar{q} \, \mathrm{d}s = 0, \qquad \forall\, \nu \in \mathcal{V}^\phi \end{aligned} \tag{2.10}$$

$$G^r[(\phi, \boldsymbol{r}), (\nu, \boldsymbol{\eta})] := \int_\Omega \eta \left\{ \frac{\partial r}{\partial t} - g(\phi, r) \right\} \mathrm{d}x = 0, \qquad \forall\, \eta \in \mathcal{V}^r \tag{2.11}$$

2.2.2. Spatial discretization using a non-conforming finite-element scheme

A Galerkin finite-element scheme to solve the weak formulation of the monodomain problem can be stated as follows. Let $\Omega^h = \cup_{e=1}^{N_{\text{el}}} \Omega_e$ be a domain discretization where N_{el} is the number of elements, and all elements comply with the condition $\Omega_i \cap \Omega_j = \emptyset$ for $i \neq j$. We construct finite-dimensional subspaces $\mathcal{S}_h^\phi \subset \mathcal{S}^\phi$, $\mathcal{S}_h^r \subset \mathcal{S}^r$ and $\mathcal{V}_h^\phi \subset \mathcal{V}^\phi$, $\mathcal{V}_h^r \subset \mathcal{V}^r$, to solve the following FE problem (Göktepe & Kuhl, 2009; Hurtado & Kuhl, 2014): $\forall\ t \in (0,T]$,

find $(\phi^h, \boldsymbol{r}^h) \in \mathcal{S}_h^\phi \times \mathcal{S}_h^r$ such that

$$G^\phi[(\phi^h, \boldsymbol{r}^h), (\nu^h, \boldsymbol{\eta}^h)] = 0, \quad \forall \nu^h \in \mathcal{V}_h^\phi$$
$$G^r[(\phi^h, \boldsymbol{r}^h), (\nu^h, \boldsymbol{\eta}^h)] = 0, \quad \forall \eta^h \in \mathcal{V}^r.$$

A traditional discretization FE scheme is the hexahedral isoparametric finite-element space,

$$\mathcal{V}_h^\phi := \left\{ \nu^h \in C^0(\Omega^h, \mathbb{R}) : \nu^h|_{\Omega_e} \in Q_k(\Omega_e), e = 1, \ldots, N_{\text{el}} \right\}$$

where $Q_k(\Omega_e)$ represents the space of isoparametric functions resulting from n-tensor product of 1-D Lagrange polynomials of order k, which are defined over the standard (isoparametric) domain $\hat{\Omega} = [-1, 1]^n$ and mapping to a hexahedral element. We expand an element $\nu^h \in \mathcal{V}_h^\phi$ as

$$\nu^h(\boldsymbol{x}) = \sum_{A=1}^{N_{\text{dofs}}} N_A(\boldsymbol{x}) \nu_A,$$

where $\{N_A\}_{a=1,N_{\text{dofs}}}$ are the basis functions, N_{dofs} is the number of element nodes with unknown degrees of freedom, and $\{\nu_A\}_{a=1,N_{\text{dofs}}}$ are the nodal coefficients. Using the same element basis functions, we expand the trial functions as

$$\phi^h(\boldsymbol{x}, t) = \sum_{A=1}^{N_{\text{dofs}}} N_A(\boldsymbol{x}) u_A(t) + u_{\text{BC}}(\boldsymbol{x}, t), \tag{2.12}$$

where $\{u_A(t)\}_{A=1,N_{\text{dofs}}}$ correspond to the nodal values of the transmembrane potential field, and $u_{\text{BC}} \in \mathcal{S}^\phi$ is a function that satisfies the boundary conditions (2.4), i.e. $u_{\text{BC}} = \bar{\phi}$ in $\partial\Omega_\phi \times (0, T]$. For simplicity, and without loss of generality, in the following we assume that $u_{\text{BC}} = 0$. To construct the elements of $\mathcal{V}_h^r$, we write

$$\boldsymbol{\eta}^h(\boldsymbol{x}) = \sum_{e=1}^{N_{\text{el}}} \sum_{q=1}^{N_{\text{q}}} M_q^e(\boldsymbol{x}) \boldsymbol{\eta}_q^e, \tag{2.13}$$

where M_q^e is a characteristic function defined by

$$M_q^e(\boldsymbol{x}) = \begin{cases} 1, \boldsymbol{x} \in \Omega_{e,q} \\ 0, \boldsymbol{x} \notin \Omega_{e,q} \end{cases} \tag{2.14}$$

and $\Omega_{e,q} \subset \Omega_e$ is the subdomain containing the $q-$quadrature point $\boldsymbol{x}_q$, and is such that $\bigcup_{q=1}^{Nq} \Omega_{e,q} = \Omega_e$ and $\Omega_{e,q} \cap \Omega_{e,q'} = \emptyset$ whenever $q \neq q'$. Analogously, we expand an element $\boldsymbol{r}^h \in \mathcal{S}_h^r$ as

$$\boldsymbol{r}^h(\boldsymbol{x}, t) = \sum_{e=1}^{N_{\mathrm{el}}} \sum_{q=1}^{N_{\mathrm{q}}} M_q^e(\boldsymbol{x}) \boldsymbol{r}_q^e(t), \tag{2.15}$$

where $\boldsymbol{r}_q^e : (0, T] \to \mathbb{R}^{\mathrm{m}}$ represents the time evolution of the state variables at the q-quadrature point.

In this work, we consider a non-conforming spatial-discretization scheme for the monodomain equations (Hurtado & Rojas, 2018). To this end, we rewrite the residuals as

$$\begin{aligned} G^{\phi}[(\phi, \boldsymbol{r}), (\nu, \boldsymbol{\eta})] = \sum_{e=1}^{N_{\mathrm{el}}} \Bigg\{ & \int_{\Omega_e} \nu \frac{\partial \phi}{\partial t} \, \mathrm{d}x + \int_{\Omega_e} \nabla \nu \cdot \mathbf{D} \nabla \phi \, \mathrm{d}x \\ & - \int_{\Omega_e} \nu f(\phi, \boldsymbol{r}) \, \mathrm{d}x + \int_{\partial \Omega_{e,q}} \nu \bar{q} \, \mathrm{d}s \Bigg\}, \end{aligned} \tag{2.16}$$

$$G^{r}[(\phi, \boldsymbol{r}), (\nu, \boldsymbol{\eta})] = \sum_{e=1}^{N_{\mathrm{el}}} \left\{ \int_{\Omega_e} \boldsymbol{\eta} \left\{ \frac{\partial \boldsymbol{r}}{\partial t} - g(\phi, \boldsymbol{r}) \right\} \mathrm{d}x \right\}, \tag{2.17}$$

and note that in such form, integrability of the trial and test functions and their weak derivatives is required only at the element level. We enhance the polynomial basis of $\mathcal{V}_h^{\phi}$ at the element level by adding polynomial terms not included in $Q_k(\Omega_e)$. To this end, we consider the non-conforming space

$$\mathcal{E}_h^{\phi} := \left\{ \beta^h : \beta^h|_{\Omega_e} \in P_{k+m}(\Omega_e) \backslash Q_k(\Omega_e) \right\}$$

where $m \in \mathbb{Z}_+$ and $P_{k+m}(\Omega_e)$ is the space of polynomial functions of degree $k + m$ defined on the standard domain $\hat{\Omega}$. We then consider enhanced test functions ν^h which we expand as

$$\nu^h(\boldsymbol{x}) = \sum_{A=1}^{N_{\mathrm{dofs}}} N_A(\boldsymbol{x}) \nu_A + \sum_{e=1}^{N_{\mathrm{el}}} \sum_{c=1}^{N_{\mathrm{nc}}} W_c^e(\boldsymbol{x}) \beta_c^e \tag{2.18}$$

where $\beta_c^e \in \mathbb{R}$ are coefficients, W_c^e are non-conforming element basis functions, and it holds that $W_c^e = 0, \boldsymbol{x} \notin \Omega^e$. Analogously, we enhance $\mathcal{S}_h^{\phi}$ with the time-dependent non-conforming

space $\mathcal{F}_h^\phi$, and expand the enhanced trial functions as

$$\phi^h(\boldsymbol{x},t) = u^h(\boldsymbol{x},t) + \alpha^h(\boldsymbol{x},t) \tag{2.19}$$

where

$$u^h(\boldsymbol{x},t) := \sum_{B=1}^{N_{\text{dofs}}} N_B(\boldsymbol{x}) u_B(t) \tag{2.20}$$

$$\alpha^h(\boldsymbol{x},t) := \sum_{e=1}^{N_{\text{el}}} \sum_{d=1}^{N_{\text{nc}}} W_d^e(\boldsymbol{x}) \alpha_d^e(t). \tag{2.21}$$

and $\alpha_d^e : (0,T] \to \mathbb{R}$ is a time-dependent coefficient that scales the non-conforming basis functions W_d^e. Substitution of approximations (2.18),(2.19),(2.13) and (2.15) into the residuals (2.16) and (2.17) yields the following semi-discrete problem: $\forall\ t \in (0,T]$, find $(u^h, \alpha^h, \boldsymbol{r}^h) \in \mathcal{S}_h^\phi \times \mathcal{F}_h^\phi \times \mathcal{S}_h^r$ such that

$$\begin{aligned}\int_\Omega N_A\{\dot{u}^h + \dot{\alpha}^h\}\mathrm{d}x + \int_\Omega \nabla N_A \cdot \mathbf{D}\nabla\{u^h + \alpha^h\}\mathrm{d}x - \int_\Omega N_A f(u^h + \alpha^h, \boldsymbol{r}^h)\mathrm{d}x \\ + \int_{\partial\Omega_q} N_A \bar{q}\ \mathrm{d}s = 0, \quad A = 1,\dots,N_{\text{dofs}},\end{aligned} \tag{2.22}$$

$$\begin{aligned}\int_{\Omega^e} W_c^e\{\dot{u}^h + \dot{\alpha}^h\}\mathrm{d}x + \int_{\Omega^e} \nabla W_c^e \cdot \mathbf{D}\nabla\{u^h + \alpha^h\}\,\mathrm{d}x \\ - \int_{\Omega^e} W_c^e f(u^h + \alpha^h, \boldsymbol{r}^h)\mathrm{d}x = 0, \quad e = 1,\dots,N_{\text{el}};\ c = 1,\dots,N_{\text{nc}},\end{aligned} \tag{2.23}$$

$$\int_{\Omega^e} M_q^e\{\dot{\boldsymbol{r}}^h - g(u^h + \alpha^h, \boldsymbol{r}^h)\}\mathrm{d}x = 0, \quad e = 1,\dots,N_{\text{el}};\ q = 1,...,N_{\text{q}} \tag{2.24}$$

2.2.3. Semi-implicit temporal discretization

To integrate (2.22), (2.23) and (2.24) in time, we consider partitioning the time interval into $[0,\dots,t_n,t_{n+1},\dots,T]$, and approximate the time-dependent coefficients $\square(t_n) \approx \square_n$. For a generic time interval $[t_n,t_{n+1}]$ we define $\Delta t := t_{n+1} - t_n$. We further group the

expansion coefficients into vectors, and write

$$\boldsymbol{u}_n = [u_{n,1}, \ldots, u_{n,N_{\text{dofs}}}]^T, \qquad \boldsymbol{\alpha}_n^e = [\alpha_{n,1}^e, \ldots, \alpha_{n,N_{\text{nc}}}^e]^T, \qquad \boldsymbol{r}_n^e = [\boldsymbol{r}_{n,1}^e, \ldots, \boldsymbol{r}_{n,N_{\text{q}}}^e]^T \tag{2.25}$$

Following a semi-implicit (SI) time-integration approach (Whiteley, 2006), time derivatives are replaced by the finite-difference approximation

$$\dot{\square}(t_{n+1}) \approx \frac{\square_{n+1} - \square_n}{\Delta t}. \tag{2.26}$$

Diffusive terms in (2.22) and (2.23) are evaluated at $t = t_{n+1}$ and the reaction terms are evaluated at $t = t_n$. Evolution equations (2.24) were integrated using an explicit Forward-Euler scheme. As a result, the incremental time update for $t = t_{n+1}$ reads:

Given $\boldsymbol{u}_n, \{\boldsymbol{\alpha}_n^e, \boldsymbol{r}_n^e\}_{e=1,\ldots,N_{\text{el}}}$, find $\boldsymbol{u}_{n+1}, \{\boldsymbol{\alpha}_{n+1}^e, \boldsymbol{r}_{n+1}^e\}_{e=1,\ldots,N_{\text{el}}}$ such that

$$\begin{aligned}
&\sum_{B=1}^{N_{\text{dofs}}} \left\{ \int_\Omega \frac{N_A N_B}{\Delta t} + \int_\Omega \nabla N_A \cdot \mathbf{D} \nabla N_B \right\} u_{n+1,B} \\
&\quad + \sum_{e=1}^{N_{\text{el}}} \sum_{d=1}^{N_{\text{nc}}} \left\{ \int_\Omega \frac{N_A W_d^e}{\Delta t} + \int_\Omega \nabla N_A \cdot \mathbf{D} \nabla W_d^e \right\} \alpha_{n+1,d}^e \\
&\quad - \left\{ \int_\Omega \frac{N_A}{\Delta t} \{u_n^h + \alpha_n^h\} + \int_\Omega N_A f(u_n^h + \alpha_n^h, \boldsymbol{r}_n^h) \right\} = 0, \quad A = 1, \ldots, N_{\text{dofs}},
\end{aligned} \tag{2.27}$$

$$\begin{aligned}
&\sum_{b=1}^{N_{\text{en}}} \underbrace{\left\{ \int_{\Omega^e} \frac{W_c^e N_b^e}{\Delta t} + \int_{\Omega^e} \nabla W_c^e \cdot \mathbf{D} \nabla N_b^e \right\}}_{=: L_{cb}^e} u_{n+1,b}^e \\
&\quad + \sum_{d=1}^{N_{\text{nc}}} \underbrace{\left\{ \int_{\Omega^e} \frac{W_c^e W_d^e}{\Delta t} + \int_{\Omega^e} \nabla W_c^e \cdot \mathbf{D} \nabla W_d^e \right\}}_{=: K_{\alpha_{cd}}^e} \alpha_{n+1,d}^e \\
&\quad - \underbrace{\left\{ \int_{\Omega^e} \frac{W_c^e}{\Delta t} \{u_n^h + \alpha_n^h\} + \int_{\Omega^e} W_c^e f(u_n^h + \alpha_n^h, \boldsymbol{r}_n^h) \right\}}_{=: p_{\alpha_c}^e} = 0 \\
&\qquad\qquad\qquad\qquad\qquad\qquad\qquad\qquad\qquad\qquad e = 1, \ldots, N_{\text{el}};\ c = 1, \ldots, N_{\text{nc}}
\end{aligned} \tag{2.28}$$

$$\int_{\Omega^e} M_q^e \left\{ \sum_{s=1}^{N_q} M_s^e \frac{r_{n+1,s}^e - r_{n,s}^e}{\Delta t} - g(u_n^h + \alpha_n^h, \boldsymbol{r}_n^h) \right\} \mathrm{d}x = 0,$$

$$e = 1, \ldots, N_{\text{el}};\ q = 1, ..., N_q, \quad (2.29)$$

where $N_b^e := N_B\Big|_{\Omega^e}$ is the restriction of the basis function to the local element domain, and u_b^e is the corresponding nodal value, where lowercase letters indicate the local degree of freedom b corresponding to its global counterpart B. At this point, we note that (2.28) can be written in matrix form as

$$\boldsymbol{L}^e \boldsymbol{u}_{n+1}^e + \boldsymbol{K}_\alpha^e \boldsymbol{\alpha}_{n+1}^e - \boldsymbol{p}_\alpha^e(\boldsymbol{u}_n^e, \boldsymbol{\alpha}_n^e, \boldsymbol{r}_n^e) = 0,$$

for $e = 1, \ldots, N_{\text{el}}$, from where we define the time update for the element non-conforming coefficient vector as

$$\boldsymbol{\alpha}_{n+1}^{e,*}(\boldsymbol{u}_{n+1}^e; \boldsymbol{u}_n^e, \boldsymbol{\alpha}_n^e, \boldsymbol{r}_n^e) := \{\boldsymbol{K}_\alpha^e\}^{-1} \boldsymbol{p}_\alpha^e(\boldsymbol{u}_n^e, \boldsymbol{\alpha}_n^e, \boldsymbol{r}_n^e) - \{\boldsymbol{K}_\alpha^e\}^{-1} \boldsymbol{L}^e \boldsymbol{u}_{n+1}^e \quad (2.30)$$

which is computed exclusively using element-level variables, given the element vector $\boldsymbol{u}_{n+1}^e$. To update the gating-variable field, we note from (2.14) that (2.29) can be solved point-wise at each quadrature point $\boldsymbol{x}_q$ inside an element, and thus is equivalent to writing

$$\frac{\boldsymbol{r}_{q,n+1}^e - \boldsymbol{r}_{q,n}^e}{\Delta t} - g(u_n^h(\boldsymbol{x}_q) + \alpha_n^h(\boldsymbol{x}_q), \boldsymbol{r}_{q,n}^e) = 0, \quad e = 1, \ldots, N_{\text{el}};\ q = 1, ..., N_q,$$

from which the (explicit) time update for the gating variables can be solved at the quadrature-point level as

$$\boldsymbol{r}_{q,n+1}^{e,*}(\boldsymbol{u}_n^e, \boldsymbol{\alpha}_n^e, \boldsymbol{r}_n^e) := \boldsymbol{r}_{q,n}^e + \Delta t\, g(u_n^h(\boldsymbol{x}_q) + \alpha_n^h(\boldsymbol{x}_q), \boldsymbol{r}_{q,n}^e). \quad (2.31)$$

We now turn to residual (2.27), and note that it can be constructed by assembling element-level nodal contributions defined by

$$R_a^{u,e} := \sum_{b=1}^{N_{\text{en}}} \underbrace{\left\{ \int_{\Omega^e} \frac{N_a N_b}{\Delta t} + \int_{\Omega^e} \nabla N_a \cdot \mathbf{D} \nabla N_b \right\}}_{:=K^e_{u_{ab}}} u^e_{n+1,b}$$
$$+ \sum_{b=1}^{N_{\text{en}}} \underbrace{\left\{ \int_{\Omega^e} \frac{N_a W_d}{\Delta t} + \int_{\Omega^e} \nabla N_a \cdot \mathbf{D} \nabla W_d \right\}}_{L^{eT}_{ad}} \alpha^e_{n+1,d}$$
$$- \underbrace{\left\{ \int_{\Omega^e} \frac{N_a}{\Delta t} \{u^h_n + \alpha^h_n\} + \int_{\Omega^e} N_a f(u^h_n + \alpha^h_n, \boldsymbol{r}^h_n) \right\}}_{:=p^e_{u_a}}, \tag{2.32}$$

which can also be written in matrix form at the element level as

$$\boldsymbol{R}^{u,e} = \boldsymbol{K}^e_u \boldsymbol{u}^e_{n+1} + \boldsymbol{L}^{eT} \boldsymbol{\alpha}^e_{n+1} - \boldsymbol{p}^e_u(\boldsymbol{u}^e_n, \boldsymbol{\alpha}^e_n, \boldsymbol{r}^e_n). \tag{2.33}$$

Substituting update (2.30) into (2.33), we obtain an element residual that only depends on $\boldsymbol{u}^e_{n+1}$ that reads

$$\boldsymbol{R}^{u,e} = \underbrace{\left(\boldsymbol{K}^e_u - \boldsymbol{L}^{eT} \left\{ \boldsymbol{K}^e_\alpha \right\}^{-1} \boldsymbol{L}^e \right)}_{\boldsymbol{A}^e} \boldsymbol{u}^e_{n+1} + \underbrace{\boldsymbol{L}^{eT} \left\{ \boldsymbol{K}^e_\alpha \right\}^{-1} \boldsymbol{p}^e_\alpha(\boldsymbol{u}^e_n, \boldsymbol{\alpha}^e_n, \boldsymbol{r}^e_n) - \boldsymbol{p}^e_u(\boldsymbol{u}^e_n, \boldsymbol{\alpha}^e_n, \boldsymbol{r}^e_n)}_{\boldsymbol{b}^e_n(\boldsymbol{u}^e_n, \boldsymbol{\alpha}^e_n, \boldsymbol{r}^e_n)} \tag{2.34}$$

As a consequence, solving residual (2.27) is equivalent to solving the matrix linear system

$$\boldsymbol{A}\boldsymbol{u}_{n+1} + \boldsymbol{b}_n = \boldsymbol{0} \tag{2.35}$$

where $\boldsymbol{A}$ and $\boldsymbol{b}_n$ are the global matrix and vector assembled from element contributions defined in (2.34). We note that (2.35) defines the time update for the global potential vector

$$\boldsymbol{u}^*_{n+1}(\boldsymbol{u}_n, \{\boldsymbol{\alpha}^e_n, \boldsymbol{r}^e_n\}_{e=1,\dots,N_{\text{el}}}) := -\boldsymbol{A}^{-1}\boldsymbol{b}_n \tag{2.36}$$

We remark that matrix $\boldsymbol{A}$ does not depend on the coefficient vectors, and therefore will take the same values for all time steps. Thus, it can be computed on a initialization stage, inverted and stored for later use in updating the potential vector. For the sake of clarity, the steps for the solving the semi-implicit scheme are summarized in Algorithm 1.

/* initialization */
$\boldsymbol{u}_0 = \boldsymbol{0}$
$\boldsymbol{r}_0 = \boldsymbol{r}_{init}$
$\boldsymbol{\alpha}^e = \boldsymbol{0}$
$\boldsymbol{A} = \boldsymbol{0}$
for $e = 1$ **to** N_{el} **do**
  Compute $\boldsymbol{K}^e_\alpha$, $\boldsymbol{K}^e_u$ and $\boldsymbol{L}^e$ (Eq. (2.28), Eq. (2.32)) and store
  Compute $\boldsymbol{A}^e$ (Eq. (2.34)) and assemble contribution to $\boldsymbol{A}$
end
Compute $\boldsymbol{A}^{-1}$ and store
/* time integration loop */
for $n = 0$ **to** N_{steps} **do**
  for $e = 1$ **to** N_{el} **do**
    Compute $\boldsymbol{b}^e(\boldsymbol{u}^e_n, \boldsymbol{\alpha}^e_n, \boldsymbol{r}^e_n)$ (Eq. (2.34)) and assemble contribution to $\boldsymbol{b}_n$
  end
  Update $\boldsymbol{u}_{n+1} = \boldsymbol{u}^*_{n+1}(\boldsymbol{u}_n, \{\boldsymbol{\alpha}^e_n, \boldsymbol{r}^e_n\}_{e=1,\dots,N_{\text{el}}}) = -\boldsymbol{A}^{-1}\boldsymbol{b}_n$
  for $e = 1$ **to** N_{el} **do**
    Update $\boldsymbol{\alpha}^e_{n+1} = \boldsymbol{\alpha}^{e,*}_{n+1}(\boldsymbol{u}^e_{n+1}; \boldsymbol{u}^e_n, \boldsymbol{\alpha}^e_n, \boldsymbol{r}^e_n)$ (see Eq. 2.30)
    for $q = 1$ **to** N_{q} **do**
      Update $\boldsymbol{r}^e_{q,n+1} = \boldsymbol{r}^{e,*}_{q,n+1}(\boldsymbol{u}^e_n, \boldsymbol{\alpha}^e_n, \boldsymbol{r}^e_n)$ (see Eq. 2.31)
    end
  end
end

Algorithm 1: Solution algorithm

2.2.4. The Q1NC element

We materialize the non-conforming scheme defined in the previous section using incompatible-modes basis functions (Wilson et al., 1973; Taylor et al., 1976), which enhance Q1 elements. We recall that the isoparametric basis functions for Q1 3D (solid) elements are

$$\hat{N}_1 = \frac{1}{8}(1-\xi_1)(1-\xi_2)(1-\xi_3), \qquad \hat{N}_2 = \frac{1}{8}(1+\xi_1)(1-\xi_2)(1-\xi_3),$$
$$\hat{N}_3 = \frac{1}{8}(1+\xi_1)(1+\xi_2)(1-\xi_3), \qquad \hat{N}_4 = \frac{1}{8}(1-\xi_1)(1+\xi_2)(1-\xi_3),$$
$$\hat{N}_5 = \frac{1}{8}(1-\xi_1)(1-\xi_2)(1+\xi_3), \qquad \hat{N}_6 = \frac{1}{8}(1+\xi_1)(1-\xi_2)(1+\xi_3),$$
$$\hat{N}_7 = \frac{1}{8}(1+\xi_1)(1+\xi_2)(1+\xi_3), \qquad \hat{N}_8 = \frac{1}{8}(1-\xi_1)(1+\xi_2)(1+\xi_3),$$

where $(\xi_1, \xi_2, \xi_3) \in \hat{\Omega} := [-1, 1]^3$, and

$$N_a^e = \hat{N}_a \circ \hat{\boldsymbol{x}}^{-1}$$

with

$$\hat{\boldsymbol{x}} = \sum_{a=1}^{8} \hat{N}_a \boldsymbol{x}_a^e,$$

where $\boldsymbol{x}_a^e$ is the vector with nodal coordinates. Incompatible modes enhance the Q1(Ω^e) element basis by adding basis functions $\{M_c^e\}_{c=1,2,3}$, with $M_c^e = \hat{M}_c \circ \hat{\boldsymbol{x}}^{-1}$, where

$$\hat{M}_1 = 1 - (\xi_1)^2, \quad \hat{M}_2 = 1 - (\xi_2)^2, \quad \hat{M}_3 = 1 - (\xi_3)^2$$

for $(\xi_1, \xi_2, \xi_3) \in \hat{\Omega}$. Table 2.1 details the number of DOFs used for the 3D elements considered in this work. Integrals have been approximated using Gaussian quadrature on the standard domain. Table 2.1 reports the quadrature rules employed in the numerical integration of Q1, Q1NC and Q2 element implementations.

Table 2.1. Element DOFs and quadrature rules employed in numerical integration of residuals and tangents. Nomenclature: DOFs = degrees of freedom, NC = incompatible mode (internal variable)

	Element DOFs	Quadrature rule
Q1	8 DOFs	$2 \times 2 \times 2 = 8$-point
Q1NC	8 DOFs + 3 IMs	$2 \times 2 \times 2 = 8$-point
Q2	27 DOFs	$3 \times 3 \times 3 = 27$-point

2.2.5. The modified Aliev-Panfilov model for transmembrane ionic current

All simulations considered the modified Aliev-Panfilov model, which accounts for physiological voltage upstroke slopes and conduction velocities (Aliev & Panfilov, 1996; Hurtado

et al., 2016), whose expressions are described below for completeness:

$$f(\phi, r) = c_1\phi(\phi - \alpha)(1 - \phi) - c_2 r\phi \tag{2.37}$$

$$g(\phi, r) = \left(\gamma + \frac{\mu_1 r}{\mu_2 + \phi}\right)(-r - c_2\phi(\phi - b - 1)) \tag{2.38}$$

where c_1, c_2, α, γ, μ_1, μ_2 and b are constants, whose values are included in Table (2.2), and are the same employed by Hurtado and Rojas (2018). To account for a steady-state regime, initial values of the recovery value where set to $r = 0.1146$.

Table 2.2. Parameter values for the modified Aliev-Panfilov model.

α	c_1	c_2	μ_1	μ_2	b	γ	$V_r[\mathrm{mV}]$	$V_p[\mathrm{mV}]$
0.05	52	8	0.1	0.3	0.25	0.002	-85	15

2.3. Results

Finite-element simulations using Q1, Q2 and Q1NC element formulations were implemented for the FI and SI time-integration schemes described in the previous section in an enhanced version of FEAP (Taylor, 2014).

2.3.1. Plane-wave tests on CV and CT

A 3D cardiac rod with a total length of $25\,\mathrm{mm}$ was discretized using regular hexahedral elements with a uniform element size, with the exception of elements adjacent to the boundary where the size was at times smaller to fit the geometry. To study the effect of the element size, simulations were carried out with mesh sizes ranging from $h = 2\,\mathrm{mm}$ to $h = 0.0156\,\mathrm{mm}$. A zero-flux boundary condition was assumed for all boundary surfaces, with exception of the left end of the rod which was stimulated with a normalized external current of $20\,\mathrm{mV/ms}$, which corresponds to $28000\,\mu\mathrm{A/cm^3}$, for $2\,\mathrm{ms}$ to elicit a plane traveling wave along the direction of the rod. A time-step size of $0.001\,\mathrm{ms}$ was set for all simulations, which is small

when compared to standard cardiac simulations using the selected ionic model (Hurtado et al., 2016). Such small time-step size is chosen to minimize the contribution of the temporal discretization error to the overall numerical error. To compute the CV, we tracked the voltage evolution on $x_1 = 18\,\mathrm{mm}$ and $x_2 = 22\,\mathrm{mm}$ and recorded the activation time, which is defined as the time when the $\phi > 0.5$ for the first time at a certain point. Then, the CV was calculated as the difference between x_2 and x_1 divided by the difference in the activation time. The results for the CV for different element sizes are shown in Figure 2.1(a). All formulations converged to a CV = $36.9\,\mathrm{cm}/s$ as the mesh size approached $h = 0.0156\,\mathrm{mm}$. CV monotonically decreased as mesh size was decreased for Q1 and Q2 formulations. The computational effort of simulations in terms of CT is reported in figure 2.1(b). We observe that the computational demand of simulations monotonically increases as the mesh size decreases, independently of the element formulation. We do observe, however, that the FI time-integration scheme always results in higher CT than the SI scheme for all element formulations considered.

To facilitate the analysis of the accuracy-efficiency trade-off of the different schemes studied, Figure 2.2 shows the CT versus the error in CV for the Q1, Q2 and Q1NC formulations for both the implicit and semi-implicit time updates. Since we seek to minimize two objective functions, namely the CT and the CV error, the Pareto frontier, defined as the set of choices that are Pareto-efficient, is included in each subfigure. The subset of the Pareto-efficient cases that correspond to the Q1NC formulation are $\{1.2, 1.5\}[\mathrm{mm}]$ and $\{1.0, 1.2, 1.5, 2.0\}[\mathrm{mm}]$ for the FI and SI cases, respectively.

2.3.2. Benchmark simulations on a cardiac cuboid

We studied the behavior of the SINCFES using as a second test case the benchmark study on a cardiac cuboid developed by (S. A. Niederer et al., 2011), and adapted to the case of the Aliev-Panfilov model by (Hurtado et al., 2016). To this end, we consider a cuboid domain with dimensions of $20 \times 7 \times 3\,\mathrm{mm}$ with cardiac fibers oriented in the longest axis direction. A subdomain with dimensions $1.5 \times 1.5 \times 1.5\,\mathrm{mm}$ located at one of the corners of the cuboid

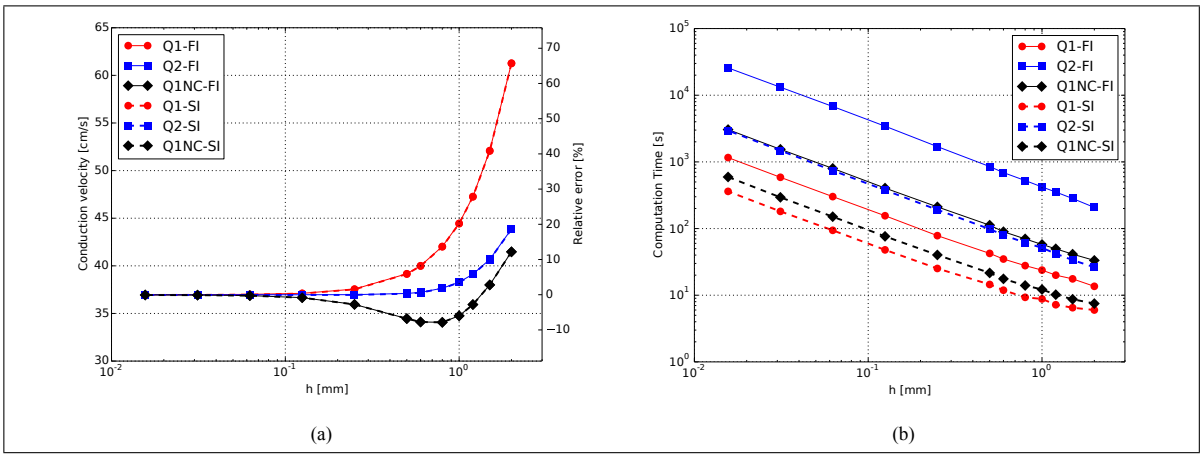

Figure 2.1. CV tests for plane-waves propagating on a 3D bar for FI and SI schemes on different element formulations. (a) Convergence study of CV as a function of the mesh size h. (b) Computational effort in terms of CT as a function of h.

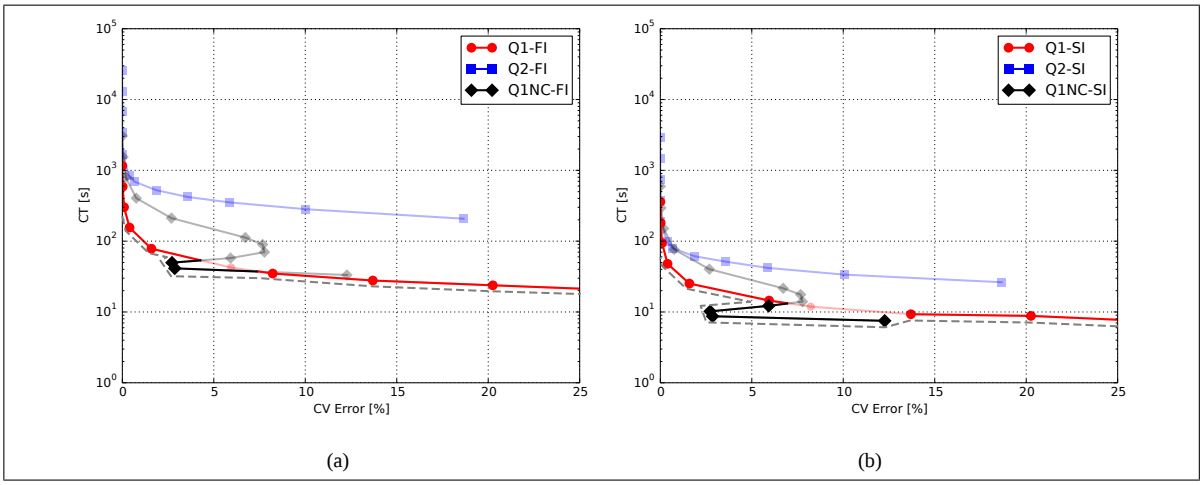

Figure 2.2. Accuracy-efficiency analysis: Computation time vs. conduction-velocity error for the different spatial discretization schemes using (a) fully-implicit time integration, and (b) semi-implicit time integration. Dashed gray line displays the Pareto frontier, which encompasses optimal cases. Suboptimal combinations are shown in transparent color.

was stimulated with an electrical current density of $50,000\,\mu\mathrm{A/cm^3}$ for $2\,\mathrm{ms}$. The normalized longitudinal and transversal conductivities were $0.0952\,\mathrm{mm^2/ms}$ and $0.0126\,\mathrm{mm^2/ms}$, respectively. Figure 2.3(a) shows the activation map and isochrones obtained on a plane that contains opposite corners in the diagonal, as defined in (S. A. Niederer et al., 2011), for a fine (Baseline) and coarse discretization using Q1 elements, and for the same coarse discretization using Q1NC elements. We note that the Q1NC case with mesh size $h = 0.8\,\mathrm{mm}$ resulted in an activation map and isochrones similar to the baseline case, defined as a Q1 model with mesh size $h = 0.1\,\mathrm{mm}$. In contrast, the activation map delivered by the Q1 coarse-mesh case with mesh size $h = 0.8\,\mathrm{mm}$ largely differed from the baseline case, delivering a less curved wave-front profile. Figure 2.3 displays the activation time values along the diagonal of the cuboid for the three cases under study. We observe that the Q1NC case closely follows the baseline case, whereas the Q1 coarse-mesh case resulted in shorter activation times at all locations along the diagonal. As a reference, the CT for the Baseline (Q1 fine), Q1NC and Q1 cases were 122,341 s, 344 s and 184 s, respectively, which is equivalent to a CT ratio of 665 : 2 : 1.

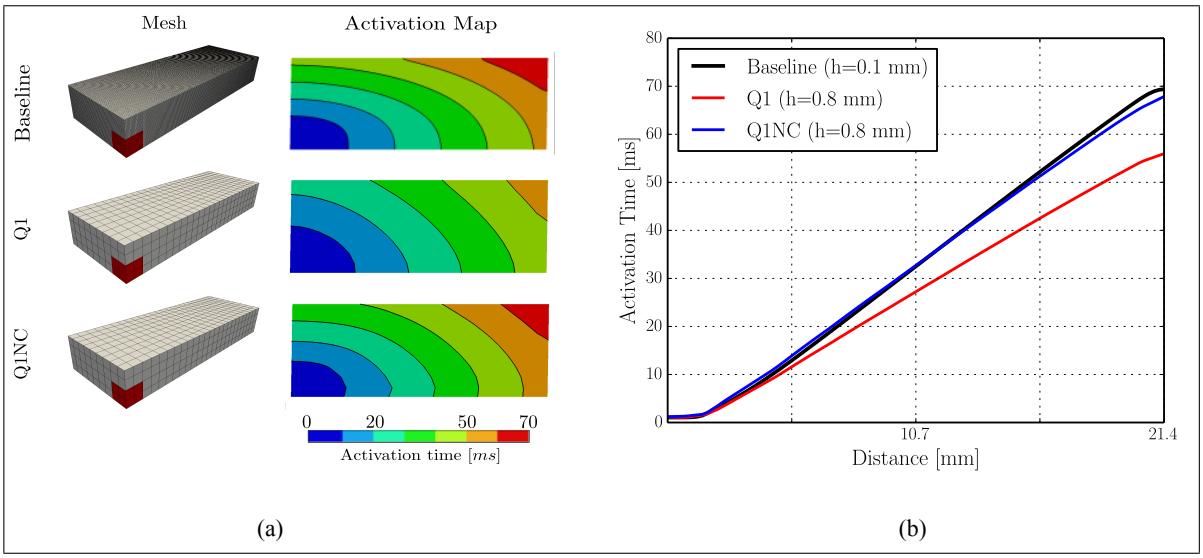

Figure 2.3. Numerical simulations on cuboid benchmark test (a) Meshes and activation maps, and (b) Activation time profile along the cuboid diagonal.

2.3.3. Biventricular human heart simulations

To study the potential of the Q1NC-SI formulation in whole-heart cardiac simulations, we modeled the propagation of an action potential on an idealized human biventricular domain stimulated at the atrio-ventricular node. The heart biventricular geometry was generated from two truncated ellipsoids (Streeter & Hanna, 1973), and later discretized using non-regular hexahedral elements. For the baseline case, a size-varying mesh with average characteristic length of $0.48\,\mathrm{mm}$ was employed. A coarse mesh with average element length of $1.0\,\mathrm{mm}$ was also considered for two additional cases with Q1 and Q1NC element formulations, see left column of Figure 2.4 for a representation of the biventricular meshes. All three cases considered the same initial boundary conditions and time step size of $0.001\,\mathrm{ms}$. The transmembrane potential distribution at different time instants during ventricular activation is depicted in Figure 2.4. We clearly observe that, as time elapses, the action-potential wave front of the Q1NC case is very similar to the Baseline case, whereas the Q1 case results in a wave front that propagates faster than the other two models due to the artificially high CV. The last column in Figure 2.4 shows the activation maps, where we observe that isochrones for the Baseline and Q1NC cases are very similar, and they both differ from the Q1 case. Biventricular simulations were ran in a HPC cluster with 128 GB of RAM memory using 32 processors using the parallel implementation of the code FEAP (Taylor, 2014). The CT for the baseline, the Q1NC and the Q1 simulation were 1805, 452 and 154 minutes respectively, which is equivalent to a CT ratio of 18 : 3 : 1.

2.3.4. Spiral wave simulations

To assess the performance of the proposed non-conforming scheme in the simulation of spiral waves, we considered a $50\,\mathrm{mm} \times 50\,\mathrm{mm}$ cardiac domain excited by means of an S1-S2 stimulation protocol. To this end, we first applied a surface stimulus (S1) of $12\,\mathrm{mV}/(\mathrm{ms}\,\mathrm{mm}^2)$ for $2\,\mathrm{ms}$ on the border defined by $x = 0$ to create a plane wave. After $280\,\mathrm{ms}$, we applied a second stimulus (S2) of $15\,\mathrm{mV}/(\mathrm{ms}\,\mathrm{mm}^3)$ in the quadrant $x < 25$, $y < 25\,\mathrm{mm}$ for $5\,\mathrm{ms}$, which resulted in the formation of a spiral wave (Sahli Costabal, Concha,

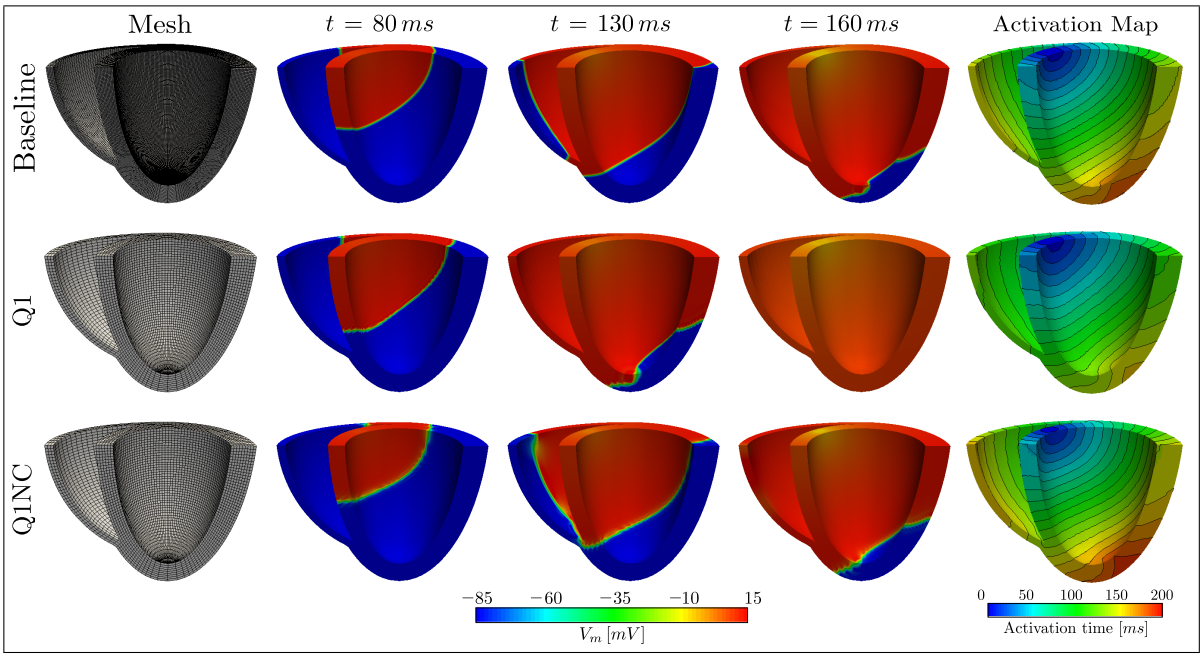

Figure 2.4. Numerical simulations on human biventricular idealized geometries. The Q1NC model displays a propagating wave similar to the baseline case during the ventricular activation sequence, whereas the Q1 model hastens the electrical stimulation ahead of the baseline case.

Hurtado, & Kuhl, 2017). This S1-S2 model was solved using three numerical models: a fine mesh with element size $h = 0.1\,\mathrm{mm}$ using Q1 elements (Baseline), a coarse mesh with element size $h = 1\,\mathrm{mm}$ using Q1 elements (Q1), and a coarse mesh with $h = 1\,\mathrm{mm}$ using the proposed non-conforming element formulation (Q1NC). In all cases, we considered a semi-implicit time update with time-step size $\Delta t = 0.005\,\mathrm{ms}$. Figure 2.5 shows the distribution of the transmembrane potential of the three models under study for several time instants. We note that at early times ($t = 110\,\mathrm{ms}$) the Q1 case displays a wave front that advanced considerably faster than the baseline and Q1NC cases. At $t = 400\,\mathrm{ms}$ a spiral wave formed in the Baseline and Q1NC cases, whereas for the Q1 case a curved wave front propagated in the outward direction but did not create a spiral. At a later instant ($t = 600\,\mathrm{ms}$), a spiral was steadily rotating in the Baseline and Q1NC cases, constantly reexciting tissue, whereas

in the Q1 case cardiac tissue was found under complete rest, and no electrical activity was observed.

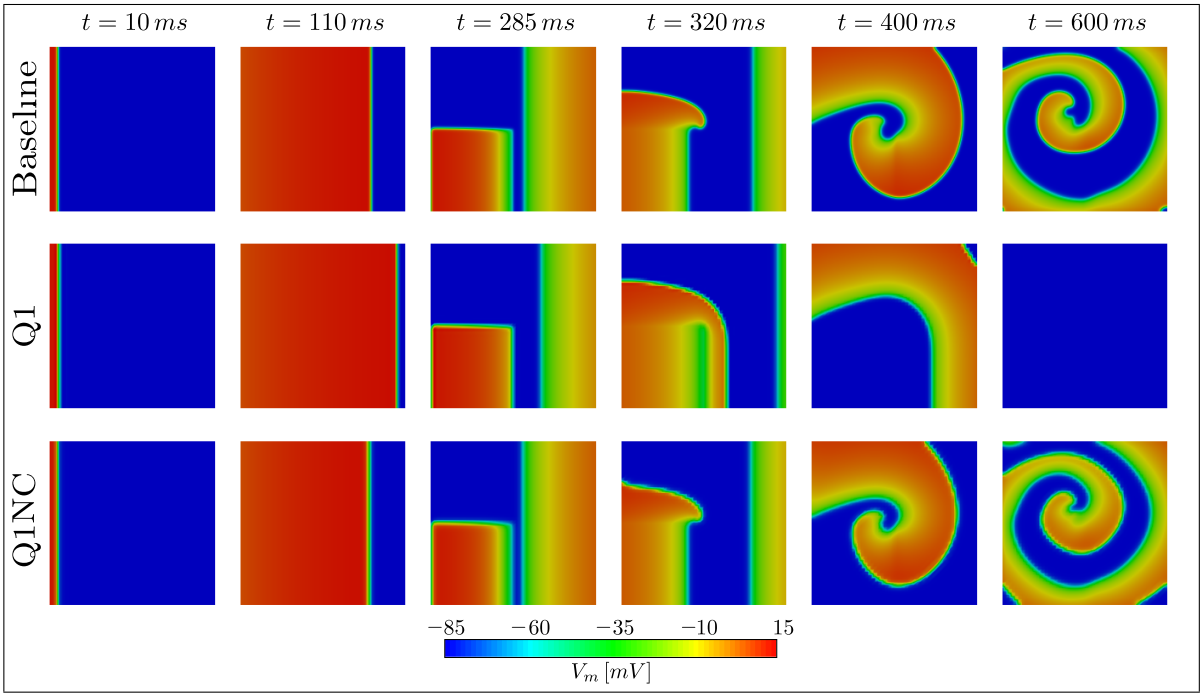

Figure 2.5. Spiral generation simulation in a 2D slab. Due to the faster CV the Q1 element is incapable of generate the spiral wave.

2.4. Discussion

In this work we have studied the features and advantages of a novel SINCFES in the solution of the monodomain model of cardiac electrophysiology. From plane-wave CV tests we note that the FI and SI schemes yield similar results for the conduction velocity for the time-step size employed, see Figure 2.1(a). This is expected, as the time-step size considered here is small compared to standard values employed in numerical simulations (Krishnamoorthi et al., 2013). Interestingly, we observe that in the case of mesh sizes $h < 0.6\,\mathrm{mm}$, the Q1, Q2 and Q1NC element formulations delivered very similar results in terms of CV error. For the

cases where $h > 0.6\,\mathrm{mm}$, the CV error incurred by the Q1 formulation grows at a much faster rate than the Q2 and Q1NC formulations. An interesting result that deserves further study is the convergence trend of the Q1NC formulation, as it is not monotonically convergent in the whole range of mesh sizes studied, and it reverts the sign of the CV error in a bounded interval of mesh sizes. A similar convergence trend has been reported in the literature for standard FE discretizations, in the context of mass-lumping techniques (Pezzuto et al., 2016), which suggest as future work a more detailed study of the effect of NC spatial discretization schemes on the stiffness and mass matrices that govern the dynamics of the problem. To better analyze the accuracy-efficiency trade-off for each scheme, we constructed CT vs CV-error plots, where the Pareto frontier has been identified. We conclude that the SINCFES delivers Pareto-optimal results for cases with mesh size in the range of $\{1.0, 1.2, 1.5, 2.0\}[\mathrm{mm}]$. For smaller mesh sizes, traditional Q1 formulations deliver better combinations of CT and CV-error than Q1NC and Q2. It is interesting to note that, in general, Q2 elements are less efficient than the Q1 and Q1NC elements from a Pareto-optimality viewpoint for the whole range of mesh sizes studied. We also note that these conclusions are particular to a plane-wave propagation case, where anisotropy of conductivity and curvature of propagating wavefronts are absent.

We further studied the performance of Q1NC elements using a benchmark problem on a cuboid cardiac domain (S. A. Niederer et al., 2011). Our simulations showed that the Q1NC formulation on a coarse mesh ($h = 0.8\,\mathrm{mm}$) can result in activation maps that are similar to those obtained on fine meshes using Q1 ($h = 0.1\,\mathrm{mm}$) , adequately capturing the anisotropic conduction of the propagating waves, see Figure 2.3(a). An analysis of the activation-time profile along the cuboid diagonal shows that the Q1NC scheme delivers an accurate conduction velocity, which is comparable to Q1 meshes with mesh sizes that are 8 times smaller, see 2.3(b). This result confirms the ability of Q1NC elements to capture the propagation of electrical waves in anisotropic media with good accuracy at significantly reduced CTs. In contrast, Q1 coarse-mesh simulations resulted in markedly higher conduction velocity profiles, and did poorly in capturing the anisotropic propagation of wavefronts when compared to the Q1NC formulation.

Numerical simulations on a biventricular domain showed that our non-conforming scheme can be effectively used in unstructured meshes of idealized anatomical geometries of the heart, see Figure 2.4. Similarly to the cardiac rod case, a coarse mesh using Q1NC elements performs much better than a simulation using standard Q1 elements on the same discretization level, as it predicts more accurately the wavefront propagation pattern, when compared to the baseline case. This conclusion is also reached from observing the resulting activation maps, where the spatial distribution and curved shape of isochrones in the Q1NC and baseline are similar, whereas the Q1 formulation delivers an isochrone distribution with lower activation-time values. We note here that this study considered an idealized and smooth geometrical representation of the ventricles of the human heart, useful for numerical verification purposes. It is important to note that such idealized domain does not include important anatomical structures such as the intricate endocardial surface, papillary muscles, and Purkinje network, that are currently included in advanced heart models (Ponnaluri et al., 2016; Sahli Costabal, Hurtado, & Kuhl, 2016). Future work should focus in understanding how non-conforming formulations can handle such fine-scale anatomical details and structures.

The performance of the SINCFES was studied in the simulation of spiral waves. Remarkably, a very coarse mesh using Q1NC elements is capable to correctly produce, and sustain in time, a spiral wave, whereas a standard Q1 formulation using the same mesh size results in no activation of cardiac tissue. The ability of SINCFES to reproduce spiral wave formation and dynamics is a key result of this work, as it shows that the method is *physically* more accurate than standard FE formulations for coarse discretizations. This result can be explained by the reduced dependance of the CV on the mesh size, and highlights the potential of the SINCFES in the simulation of cardiac arrhythmias, the main clinical focus of cardiac electrophysiology simulations. While spiral patterns and dynamics obtained with the Q1NC formulation are very similar to the baseline results, a time delay is observed for the former, which resulted in differences in the spatial distribution of the transmembrane voltage, see last column of Figure 2.5. Such delay, which can ultimately be attributed to differences in the local CV, has also been observed in studies employing very high-order space-time formulations (Coudière &

Turpault, 2017), confirming that state-of-the-art simulations of spirals using standard values of mesh size and time step are also affected by this time delay. Despite this persistent numerical error, we believe that the focus of future studies should be in recovering the overall dynamical features of spirals, i.e spiral tip trajectories (Fenton & Karma, 1998; Gizzi et al., 2013).

We close by noting that while whole-heart simulations reported in the literature predominantly employ tetrahedral discretizations, effective methods for generating patient-specific hexahedral meshes are currently available (Lamata et al., 2011). Further, hexahedral meshes have gained great attention in the context of cardiac simulations, as the numerical performance of hexahedral elements is superior to tetrahedral elements when solving mechanics of the heart, particularly under the assumption of incompressible and quasi-incompressible regimes (Hadjicharalambous, Lee, Smith, & Nordsletten, 2014). As a conclusion, a natural continuation of this work is the application of non-conforming schemes in the solution of electromechanical models of the heart (Nash & Panfilov, 2004). One important reason for mesh-coarsening FE models of the heart is to reduce the number of DOFs, which in the case of electromechanical cardiac models is much larger than in pure electrophysiological simulations, as displacement, fiber stretch/stress variables, and the non-linearity of tissue constitutive models drastically increase the dimensionality and computational effort needed to solve the governing equations (Göktepe & Kuhl, 2010; Hurtado, Castro, & Madrid, 2017).

3. CONCLUSIONS

In this thesis we have developed a non-conforming semi-implicit finite element scheme (SINCFES) for the numerical solution of the electrophysiology equations that model the electrical activity of the heart. Through numerical simulations, we have shown that the proposed method captures the cardiac electrical frontwave better than traditional low-order Lagrange finite elements without increasing the computational cost. In particular, we demonstrated the capabilities of the proposed method by performing 3D plane wave simulations, were the conduction velocity was monitored. We found that the proposed method is Pareto-optimal for mesh sizes larger than 1.0 mm. In a more demanding simulation a slab of anisotropic cardiac tissue was stimulated and the activation times were recorded. The non-conforming method captures better the curvature of the wave and a accurate conduction velocity along the diagonal of the cuboid than the traditional Q1.

The SINCFES was also tested in a simplified biventricular domain in an effort to predict the performance of the method in a realistic geometry. As expected, the Q1NC element reproduces better the wavefront than the Q1 element for a coarser mesh when compared to a baseline computed with finer elements. Finally, we performed a 2D simulation of a cardiac spiral and contrast the performance of the traditional Q1 element with the Q1NC element in a coarse mesh. For the same excitation protocol, the Q1NC success to capture the formation of a spiral wave that is similar to the baseline case. in constrast, simulations using Q1 element with the same mesh size do not capture the formation of spiral waves.

4. FUTURE WORK

The present work opens the door to several questions and research opportunities. We have demonstrated that Q1NC elements allow us to use coarser meshes without considerably increasing the computational cost and without losing accuracy. Therefore, most of the future work is focused on evaluating the performance of the method in physiological phenomena. For example, in this work we study the ability of the Q1NC to reproduce a simple spiral wave, which is a simplification of arrhythmias in the heart. Future efforts should extend these results by studying how the SINCFES behaves in the simulation of different arrhythmogenic cases, such as those described in Fenton and Karma (1998). In particular, a relevant study is the assessment of the SINCFES in capturing the evolution of spiral-wave tips, which have been related to the nature of cardiac pathologies.

Another avenue to future research is the study of how important electrophysiological quantities other than the transmembrane potential are captured in simulations with biophysical ionic models solved using the SINCFES. Two such electrophysiological parameters are the action-potential duration (APD) and the repolarization time (RT) (Fenton & Karma, 1998). These two are important to account for the physiological accuracy of a simulation, and will display very different behavior depending on the electrophysiology model selected for the ionic transmembrane current. We note here that the model employed in this work, the Aliev-Panfilov model, represents a convenient phenomenological model that only has two variables, but it fails to captures important electrophysiological features (Tusscher et al., 2004). Future developments of the SINCFES should include the use of biophysical models of ionic transmembrane current, as well as the use of more realistic geometries of the heart chambers.

In this work we have considered the enhancement of linear finite-element formulations using non-conforming modes. A natural question is how higher-order elements can benefit

from the non-conforming approach. For example, an immediate extension is the development of Q2 non-conforming elements, which enrich second-order Lagrange elements with third order basis functions. The use of traditional higher-order finite-element formulations has been explored in the past, displaying interesting properties and benefits from a computational point of view (Arthurs et al., 2012; Vincent et al., 2015).

To close, we think that the most important future work, and where we believe that the SINCFES can contribute the most, is to apply the SINCFES to the numerical solution of cardiac electromechanical models that simulate both the electrical propagation and mechanical contraction of the cardiac tissue simultaneously. This problems are computationally very challenging, as the transmembrane potential field is complemented with the displacement field, increasing the dimension of the mathematical formulation, and at the same time increasing the computational complexity, as more degrees of freedom are needed in each node to solve for this multi-field problem.

BIBLIOGRAPHY

Aliev, R. R., & Panfilov, A. V. (1996). A Simple Two-variable Model of Cardiac Excitation. *Chaos, Solitons and Fractals*, *7*(3), 293–301.

Arthurs, C. J., Bishop, M. J., & Kay, D. (2012). Efficient simulation of cardiac electrical propagation using high order finite elements. *Journal of Computational Physics*, *231*(10), 3946–3962.

Cantwell, C. D., Yakovlev, S., Kirby, R. M., Peters, N. S., & Sherwin, S. J. (2014). High-order spectral/hp element discretisation for reaction-diffusion problems on surfaces: Application to cardiac electrophysiology. *Journal of Computational Physics*, *257*, 813–829.

Castro, S. (2015). *Multiscale modeling of cardiac electrophysiology: A non-linear diffusion approach to the electrical excitation of cardiac tissue* (Unpublished master's thesis). Pontificia Universidad Católica de Chile.

Colli Franzone, P., Pavarino, L. F., & Scacchi, S. (2014). *Mathematical Cardiac Electrophysiology* (Vol. 13). Retrieved from `http://link.springer.com/10.1007/978-3-319-04801-7` doi: 10.1007/978-3-319-04801-7

Coudière, Y., & Turpault, R. (2017). Very high order finite volume methods for cardiac electrophysiology. *Computers and Mathematics with Applications*, *74*(4), 684–700. Retrieved from `http://dx.doi.org/10.1016/j.camwa.2017.05.012` doi: 10.1016/j.camwa.2017.05.012

Dupraz, M., Filippi, S., Gizzi, A., Quarteroni, A., & Ruiz-Baier, R. (2015). Finite element and finite volume-element simulation of pseudo-ECGs and cardiac alternans. *Mathematical Methods in the Applied Sciences*, *38*(6), 1046–1058. doi: 10.1002/mma.3127

Fenton, F. H., & Karma, A. (1998). Vortex dynamics in three-dimensional continous myocardium with fiber rotation: Filament instablity and fibrillation. *Chaos*, *8*(1), 20–47. doi: 10.1063/1.166374

Gizzi, A., Cherry, E. M., Gilmour, R. F., Luther, S., Filippi, S., & Fenton, F. H. (2013). Effects of pacing site and stimulation history on alternans dynamics and the development of complex spatiotemporal patterns in cardiac tissue. *Frontiers in Physiology*, *4 APR*(April), 1–20. doi: 10.3389/fphys.2013.00071

Göktepe, S., & Kuhl, E. (2009). Computational modeling of cardiac electrophysiology: A novel finite element approach. *International Journal for Numerical Methods in Engineering*.

Göktepe, S., & Kuhl, E. (2010). Electromechanics of the heart: A unified approach to the strongly coupled excitation-contraction problem. *Computational Mechanics*, *45*(2-3), 227–243. doi: 10.1007/s00466-009-0434-z

Guyton, A. C., & Hall, J. E. (2016). *Textbook of medical physiology*. Elsevier.

Hadjicharalambous, M., Lee, J., Smith, N. P., & Nordsletten, D. A. (2014). A displacement-based finite element formulation for incompressible and nearly-incompressible cardiac mechanics. *Computer Methods in Applied Mechanics and Engineering*, *274*, 213–236. Retrieved from `http://dx.doi.org/10.1016/j.cma.2014.02.009` doi: 10.1016/j.cma.2014.02.009

Hodgkin, A. L., & Huxley, A. F. (1952). A quantitative description of membrane current and its application to conduction and excitation in nerve. *Journal of Physiology*, *117*(4), 500–544. doi: 10.1007/BF02459568

Hughes, T. J. (2012). *The finite element method: linear static and dynamic finite element analysis*. Courier Corporation.

Hurtado, D. E., Castro, S., & Gizzi, A. (2016). Computational modeling of non-linear diffusion in cardiac electrophysiology: A novel porous-medium approach. *Computer Methods in*

Applied Mechanics and Engineering, *300*, 70–83. doi: 10.1016/j.cma.2015.11.014

Hurtado, D. E., Castro, S., & Madrid, P. (2017). Uncertainty quantification of two models of cardiac electromechanics. *International Journal for Numerical Methods in Biomedical Engineering*, *e2984*, 1–21. Retrieved from http://doi.wiley.com/10.1002/cnm.2894 doi: 10.1002/cnm.2894

Hurtado, D. E., & Henao, D. (2014). Gradient flows and variational principles for cardiac electrophysiology: Toward efficient and robust numerical simulations of the electrical activity of the heart. *Computer Methods in Applied Mechanics and Engineering*, *273*, 238–254.

Hurtado, D. E., & Kuhl, E. (2014). Computational modelling of electrocardiograms: repolarisation and T-wave polarity in the human heart. *Computer methods in biomechanics and biomedical engineering*, *17*(9), 986–96. Retrieved from http://www.ncbi.nlm.nih.gov/pubmed/23113842 doi: 10.1080/10255842.2012.729582

Hurtado, D. E., & Rojas, G. (2018). Non-conforming finite-element formulation for cardiac electrophysiology: an effective approach to reduce the computation time of heart simulations without compromising accuracy. *Computational Mechanics*, *61*(4), 485–497. Retrieved from http://link.springer.com/10.1007/s00466-017-1473-5 doi: 10.1007/s00466-017-1473-5

Keener, J., & Sneyd, J. (2009a). *Mathematical Physiology: I: Cellular Physiology*. Springer New York. doi: https://doi.org/10.1007/978-0-387-79388-7

Keener, J., & Sneyd, J. (2009b). *Mathematical Physiology: II: Systems Physiology*. Springer New York. doi: https://doi.org/10.1007/978-0-387-79388-7

Krishnamoorthi, S., Sarkar, M., & Klug, W. S. (2013). Numerical quadrature and operator splitting in finite element methods for cardiac electrophysiology. *International Journal for Numerical Methods in Biomedical Engineering*, *29*, 1243–1266.

Lamata, P., Niederer, S. A., Nordsletten, D., Barber, D. C., Roy, I., Hose, D. R., & Smith,

N. (2011). An accurate, fast and robust method to generate patient-specific cubic Hermite meshes. *Medical Image Analysis*, *15*(6), 801–813. Retrieved from http://dx.doi.org/10.1016/j.media.2011.06.010 doi: 10.1016/j.media.2011.06.010

Nash, M. P., & Panfilov, A. V. (2004). Electromechanical model of excitable tissue to study reentrant cardiac arrhythmias. *Progress in Biophysics and Molecular Biology*, *85*(2-3), 501–522.

Niederer, S., Mitchell, L., Smith, N., & Plank, G. (2011). Simulating human cardiac electrophysiology on clinical time-scales. *Frontiers in Physiology*, *APR*(April). doi: 10.3389/fphys.2011.00014

Niederer, S. A., Kerfoot, E., Benson, a. P., Bernabeu, M. O., Bernus, O., Bradley, C., ... Smith, N. P. (2011). Verification of cardiac tissue electrophysiology simulators using an N-version benchmark. *Philosophical Transactions of the Royal Society A: Mathematical, Physical and Engineering Sciences*, *369*(1954), 4331–4351. doi: 10.1098/rsta.2011.0139

Pathmanathan, P., Bernabeu, M. O., Bordas, R., Cooper, J., Garny, A., Pitt-Francis, J. M., ... Gavaghan, D. J. (2010). A numerical guide to the solution of the bidomain equations of cardiac electrophysiology. *Progress in Biophysics and Molecular Biology*, *102*(2-3), 136–155. Retrieved from http://dx.doi.org/10.1016/j.pbiomolbio.2010.05.006 doi: 10.1016/j.pbiomolbio.2010.05.006

Pezzuto, S., Hake, J., & Sundness, J. (2016). Space-discretization error analysis and stabilization schemes for conduction velocity in cardiac electrophysiology. *International Journal for Numerical Methods in Biomedical Engineering*, *32*(10), e02762–n/a.

Ponnaluri, A. V., Perotti, L. E., Liu, M., Qu, Z., Weiss, J. N., Ennis, D. B., ... Garfinkel, A. (2016). Electrophysiology of Heart Failure Using a Rabbit Model: From the Failing Myocyte to Ventricular Fibrillation. *PLoS Computational Biology*, *12*(6), 1–25. doi: 10.1371/journal.pcbi.1004968

Pullan, A. J., Cheng, L. K., & Buist, M. L. (2005). *Mathematically modelling the electrical activity of the heart: From cell to body surface and back again*. World Scientific.

Rojas, G. (2017). *Incompatible modes finite-element formulation for cardiac electrophisiology: An efficient approach to coarsening heart simulations without compromising accuracy* (Unpublished master's thesis). Pontificia Universidad Catolica de Chile.

Sahli Costabal, F., Hurtado, D. E., & Kuhl, E. (2016). Generating Purkinje networks in the human heart. *Journal of Biomechanics*, *49*, 2455–2465.

Sahli Costabal, F., Yao, J., & Kuhl, E. (2018). Predicting drug-induced arrhythmias by multiscale modeling. *International Journal for Numerical Methods in Biomedical Engineering*, 1–21. Retrieved from `http://doi.wiley.com/10.1002/cnm.2964` doi: 10.1002/cnm.2964

Sahli Costabal, F., Concha, F., Hurtado, D., & Kuhl, E. (2017). The importance of mechano-electrical feedback and inertia in cardiac electromechanics. *Computer Methods in Applied Mechanics and Engineering*, *320*, 352–368.

Streeter, D. D., & Hanna, W. T. (1973). Engineering mechanics for successive states in canine left ventricular myocardium: I. Cavity and wall geometry. *Circulation Research*, *33*, 639–655.

Sundnes, J., Lines, G. T., Cai, X., Nielsen, B. F., Mardal, K. A., & Tveito, A. (2006). *Computing the Electrical Activity in the Heart*. Berlin Heidelberg: Springer-Verlag.

Taylor, R. L. (2014). *FEAP - finite element analysis program.* University of California, Berkeley. Retrieved from `http://www.ce.berkeley/feap`

Taylor, R. L., Beresford, P. J., & Wilson, E. L. (1976). A Nonconforming Element for Stress Analysis. *International Journal for Numerical Methods in Engineering*, *10*, 1211-1219.

Trayanova, N. A., Boyle, P. M., & Nikolov, P. P. (2018). Personalized imaging and modeling

strategies for arrhythmia prevention and therapy. *Current Opinion in Biomedical Engineering*, *5*, 21–28. Retrieved from http://linkinghub.elsevier.com/retrieve/pii/S2468451117300922 doi: 10.1016/j.cobme.2017.11.007

Tusscher, K. H. W. J., Noble, D., Noble, P. J., & Panfilov, A. V. (2004). A model for human ventricular tissue. *AJP - Heart and Circulatory Physiology*, *286*(4), 1573–1589. doi: 10.1152/ajpheart.00794.2003

Vadakkumpadan, F., Rantner, L. J., Tice, B., Boyle, P., Prassl, A. J., Vigmond, E., ... Trayanova, N. A. (2009). Image-based models of cardiac structure with applications in arrhythmia and defibrillation studies. *Journal of Electrocardiology*, *42*(2), 157.e1–157.e10. Retrieved from http://dx.doi.org/10.1016/j.jelectrocard.2008.12.003 doi: 10.1016/j.jelectrocard.2008.12.003

Vazquez, M., Aris, R., Houzeaux, G., Aubry, R., Villar, P., Garcia-Barnes, J., ... Carreras, F. (2011). A massively parallel computational electrophysiology model of the heart. *International Journal for Numerical Methods in Biomedical Engineering*, *27*, 1911–1929.

Vincent, K. P., Gonzales, M. J., Gillette, A. K., Villongco, C. T., Pezzuto, S., Omens, J. H., ... McCulloch, A. D. (2015). High-order finite element methods for cardiac monodomain simulations. *Frontiers in Physiology*, *6*(Aug), 1–9.

Whiteley, J. P. (2006). An efficient numerical technique for the solution of the monodomain and bidomain equations. *IEEE Transactions on Biomedical Engineering*, *53*(11), 2139–2147. doi: 10.1109/TBME.2006.879425

Wilson, E. L., Taylor, R. L., Doherty, W. P., & Ghaboussi, J. (1973). Incompatible Displacement Models. In *Numerical and computer methods in structural mechanics.* Academic Press.

Ying, W., Rose, D. J., & Henriquez, C. S. (2008). Efficient fully implicit time integration methods for modeling cardiac dynamics. *IEEE Transactions on Biomedical Engineering*,

55(12), 2701–2711. doi: 10.1109/TBME.2008.925673